arXiv:1404.6795v2 [astro-ph.GA] 3 May 2014

Evidence for AGN Feedback in the Broad Absorption Lines and Reddening of Mrk 231[1,2]

Karen M. Leighly[3,4]

Homer L. Dodge Department of Physics and Astronomy, The University of Oklahoma, 440 W. Brooks St., Norman, OK 73019

Donald M. Terndrup[3]

Department of Astronomy, The Ohio State University, 140 W. 18th Ave., Columbus, OH 43210

Eddie Baron

Homer L. Dodge Department of Physics and Astronomy, The University of Oklahoma, 440 W. Brooks St., Norman, OK 73019

Adrian B. Lucy

Homer L. Dodge Department of Physics and Astronomy, The University of Oklahoma, 440 W. Brooks St., Norman, OK 73019

Matthias Dietrich[3,4]

Department of Physics and Astronomy, Ohio University, Clippinger Labs 251B, Athens, OH 45701

and

Sarah C. Gallagher

Department of Physics & Astronomy, The University of Western Ontario, London, ON, N6A 3K7, Canada

Received _____; accepted _____

Resubmitted to ApJ

ABSTRACT

We present the first J-band spectrum of Mrk 231, which reveals a large He I*λ10830 broad absorption line with a profile similar to that of the well-known Na I broad absorption line. Combining this spectrum with optical and UV spectra from the literature, we show that the unusual reddening noted by Veilleux et al. (2013) is explained by a reddening curve like those previously used to explain low values of total-to-selective extinction in SNe Ia. The nuclear starburst may be the origin and location of the dust. Spatially-resolved emission in the broad absorption line trough suggests nearly full coverage of the continuum emission region. The broad absorption lines reveal higher velocities in the He I* lines (produced in the quasar-photoionized H II region) compared with the Na I and Ca II lines (produced in the corresponding partially-ionized zone). *Cloudy* simulations show that a density increase is required between the H II and partially-ionized zones to produce ionic column densities consistent with the optical and IR absorption line measurements and limits, and that the absorber lies $\sim 100\,\mathrm{pc}$ from the central engine. These results suggest that the He I* lines are produced in an ordinary quasar BAL wind that impacts upon, compresses, and accelerates the nuclear starburst's dusty effluent (feedback in action), and the Ca II and Na I lines are produced in this dusty accelerated gas. This unusual circumstance explains the rarity of Na I absorption lines; without the compression along our line of sight, Mrk 231 would appear as an ordinary FeLoBAL.

Subject headings: quasars: absorption lines — quasars: individual (Mrk 231)

1. Introduction

Mrk 231 is a nearby ($z = 0.0421$) ultraluminous infrared galaxy that has a Seyfert 1 optical spectrum (Sanders et al. 1988). The infrared emission is thought to be a combination of AGN and starburst activity (e.g., Farrah et al. 2003, and references therein). Recently, attention has been again drawn to this galaxy as a consequence of the discovery of a powerful, wide-angle, kiloparsec-scale molecular outflow (Rupke & Veilleux 2011).

Mrk 231's optical spectrum shows extreme Fe II emission, undetected [O III]$\lambda\lambda$4959, 5007, and somewhat broad and prominent Balmer lines. The most remarkable feature is the very strong broad Na ID absorption line with $v \approx -4,500\,\mathrm{km\,s^{-1}}$ (Adams & Weedman 1972; Boksenberg et al. 1977; Rudy et al. 1985; Schmidt & Miller 1985; Hamilton & Keel 1987; Boroson et al. 1991; Kollatschny et al. 1992; Forster et al. 1995; Rupke et al. 2002; Gallagher et al. 2005; Lípari et al. 2005; Rupke et al. 2005; Rodríguez Zaurín et al. 2009; Veilleux et al. 2013), not to be confused with the few-hundred $\mathrm{km\,s^{-1}}$ Na ID absorption consistent with the velocity of the molecular outflow (Rupke et al. 2005). While low-velocity

---

[1]This work is based on observations obtained at the MDM Observatory, operated by Dartmouth College, Columbia University, Ohio State University, Ohio University, and the University of Michigan.

[2]Based on observations obtained with the Apache Point Observatory 3.5-meter telescope, which is owned and operated by the Astrophysical Research Consortium.

[3]Visiting Astronomer at the Infrared Telescope Facility, which is operated by the University of Hawaii under Cooperative Agreement no. NNX-08AE38A with the National Aeronautics and Space Administration, Science Mission Directorate, Planetary Astronomy Program.

[4]Visiting Astronomer, Kitt Peak National Observatory, which is operated by the Association of Universities for Research in Astronomy (AURA) under cooperative agreement with the National Science Foundation.

Na ID absorption from molecular outflows is relatively common (e.g., Rupke et al. 2005), high-velocity, broad absorption Na ID lines are rare. The Na ID absorption is accompanied by Ca IIλ3935, 3970 and He I*λ3889 in the optical bandpass (e.g., Adams & Weedman 1972; Boksenberg et al. 1977; Rudy et al. 1985; Schmidt & Miller 1985; Hutchings & Neff 1987; Boroson et al. 1991; Rupke et al. 2002; Lípari et al. 2005; Rodríguez Zaurín et al. 2009; Veilleux et al. 2013). Near-UV and UV broad absorption lines were reported by Smith et al. (1995) and Gallagher et al. (2005).

The broad absorption lines classify Mrk 231 as a broad absorption line Quasar (BALQSO). Broad absorption line quasars constitute between 10 and 40% of quasars, depending on selection criteria (e.g., Hewett & Foltz 2003; Trump et al. 2006; Dai et al. 2008). Mrk 231 also exhibits Fe II broad absorption lines, making Mrk 231 the nearest iron low-ionization broad absorption line quasar (FeLoBAL). FeLoBALs are much rarer than BALQSOs, constituting only $\sim 2\%$ of quasars, and again, the rate of incidence measured depends on the sample selection (Urrutia et al. 2009; Dai et al. 2012). BALQSOs have drawn intense interest in recent years, as their outflows may be key for understanding AGN feedback, i.e., the process by which an AGN influences its host galaxy, specifically, how does the outflow act to supress specifically, how it acts to suppress the rate of star formation in the host; see, for example, Farrah et al. (2012) who provides a discusison of the problem, and also has recently found evidence for an anticorrelation between the strength of the broad absorption-line outflow and the fractional contribution from star formation to the IR luminosity in a sample of FeLoBALs; they interpret this result as evidence for the AGN outflow curtailing star formation in the host galaxy.

As noted by Veilleux et al. (2013), the presence of He I*λ3889 and Na I in the same outflow appears to be problematic from a photoionization point of view. Metastable He I* is formed by recombination onto He^+, and so it occurs in the H II region of the outflow,

in roughly the same gas that would generate C IV (e.g., Leighly et al. 2011). In contrast, neutral sodium has an ionization potential of only 5.14 eV, i.e., less than that of hydrogen, so must occur in the partially-ionized zone beyond the hydrogen ionization front. It is distinguished from other low-ionization absorption lines such as Fe II that are formed in the partially-ionized zone, however. As shown in Lucy et al. (2014), copious Fe II is produced just past the hydrogen ionization front; Na ID is produced in basically neutral gas, much deeper in the slab, and farther from the illuminated face. Thus, He I* and Na I cannot be produced in gas with even close to the same ionization state, and so it is not necessarily easy to see how they can exhibit the same dynamics.

Mrk 231 also has an unusual optical/UV continuum spectrum (Smith et al. 1995; Veilleux et al. 2013). Specifically, while the optical spectrum shows only modest reddening, the spectrum falls steeply in the near UV, and levels out shortward of ~ 2400Å. Anomalously steep reddening has been seen in several BALQSOs (Hall et al. 2002; Leighly et al. 2009; Jiang et al. 2013), but the mechanism for this reddening remains unexplained.

In the paper, we present new infrared spectra from Mrk 231. While Mrk 231 has been observed often in the infrared, a careful search of the literature revealed no previously published J-band spectra. Our spectrum reveals, for the first time, the broad He I*λ10830 absorption line (§2.1). We also find evidence for the appearance of a new He I*λ10830 velocity component at $11,520\mathrm{km\,s^{-1}}$ (§2.2, §2.3). We present new, high signal-to-noise-ratio blue optical spectra (§2.4). Combining our data with published spectra (§2.5), we present an analysis of the reddening in this object, finding that the unusual spectral shape is consistent with so-called "circumstellar reddening" (to be defined and discussed in §3). §4 presents an analysis of the spectra, and extraction of the He I* and Ca II line profiles, which we compare with a Na I profile obtained from the literature. After introducing a physical scenario for the absorption lines in §6.2, we present in §6.3 a simple photoionization model,

using *Cloudy*, that yields the ionic column densities required to produce the observed absorption lines. We systematically investigate the assumptions of our model, within the limitations of *Cloudy* in §7 and provide an optimal model in §8. The results are summarized in §9.

2. Observations and Data

2.1. IRTF SpeX Observation

Mrk 231 was observed using SpeX (Rayner et al. 2003) on the NASA Infrared Telescope Facility (IRTF) on April 24, 2010 for 30 minutes. A standard ABBA integration scheme was used. The A0 star HD 112623 was used for flux and telluric corrections. The spectra were reduced, and the telluric correction applied, in the standard manner using Spextool and accompanying software (Cushing et al. 2004; Vacca et al. 2003). The resolution measured from the arc lamp lines was about 12Å FWHM, or $330\,\mathrm{km\,s^{-1}}$ in the vicinity of the absorption line. The spectrum is shown in Fig. 1. The galactic reddening in the direction of Mrk 231 is $E(B-V) = 0.0095$, and we correct for that using the CCM reddening curve (Cardelli et al. 1988).

We used narrow [Fe II] emission lines at 12567 and 16435Å to simultaneously check the wavelength calibration and the redshift. These lines originate in the starburst (e.g., Martins et al. 2013) and therefore should provide a good estimate of the systemic velocity. These lines yielded redshifts of 0.04248 and 0.04252, so we corrected the spectrum using the effective redshift of 0.0425. Veilleux et al. (2013) mention that the redshift of Mrk 231 is 0.0422, and that value is considered to be very accurate since it is measured from the H I 21-cm absorption feature. Our value differs from that one by $\sim 90\,\mathrm{km\,s^{-1}}$, and is therefore consistent considering the resolution of the spectrum.

Table 1. IRTF Spectrum

Observed Wavelength (μm)	Flux Density[a] (10^{-17} erg s^{-1} cm^{-2} Å^{-1})	Flux Density Error[a] (10^{-17} erg s^{-1} cm^{-2} Å^{-1})
0.805413	988.822	10.4281
0.805616	994.342	10.8305
0.805818	988.422	10.5220
0.806020	987.099	10.8525
0.806223	971.811	10.6738

Note. — Table 1 is published in its entirety in the electronic edition of the *Astrophysical Journal*. A portion is shown here for guidance regarding its form and content.

[a]Corrected for Galactic extinction.

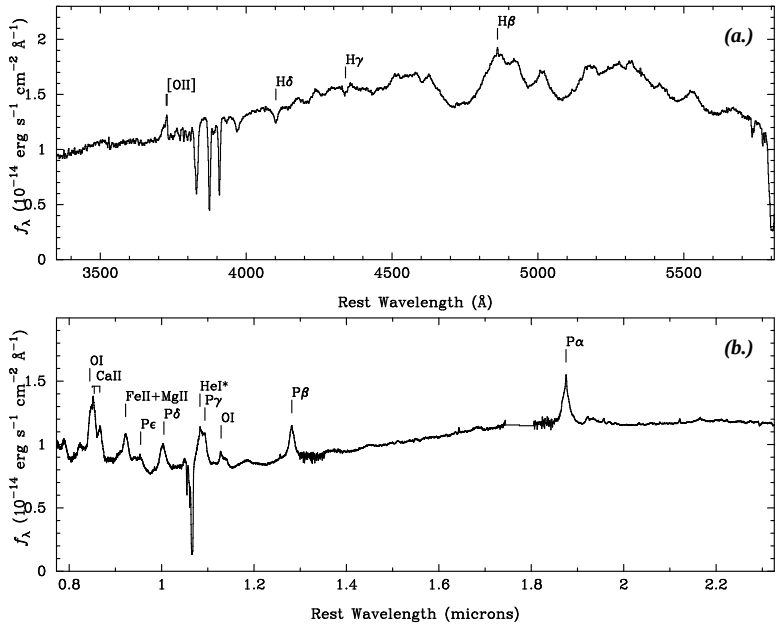

Fig. 1.— *(a.)* The KPNO spectrum of Mrk 231. Principal emission lines are marked; much of the remaining line emission is Fe II with some host galaxy emission (see also Fig. 6). Higher Balmer series lines appear as absorption lines, stemming from the contribution of the nuclear starburst (§4.1). *(b.)* The IRTF spectrum of Mrk 231. Principal lines are marked; some of the remaining features originate in the host galaxy (see also Fig. 7). Both spectra have been corrected for Galactic reddening and redshift.

We provide the observed-frame spectrum, corrected for Galactic reddening and normalized to $10^{-17}\,\mathrm{erg\,cm^{-2}\,s^{-1}\,\AA^{-1}}$ in Table 1.

2.2. MDM TIFKAM Observation

Mrk 231 has been found to demonstrate variability in the Na ID line, particularly in the $\sim 8000\,\mathrm{km\,s^{-1}}$ component (Boroson et al. 1991; Kollatschny et al. 1992; Forster et al. 1995). To check for variability in the He I*λ10830 absorption complex since our IRTF

observation in 2010, we obtained J-band spectra of Mrk 231 on the night of UT 25 March 2013 using the TIFKAM infrared imager/spectrograph (Pogge et al. 1998) on the 2.4 m Hiltner telescope of the MDM Observatory. The spectrograph delivered a resolution of 4.24 Å pixel^{-1}. The slit width was $0\farcs6$, and the effective resolution as measured from arc lamp and night sky lines was 2.2 pixels, or $\sim 260\,\mathrm{km\,s^{-1}}$ at the location of the He I* line. We obtained 13 exposures of Mrk 231, each with an exposure time of 300 s. The A0 star HD 99966 was used for flux and telluric corrections, and was observed 16×30 s at a similar airmass to Mrk 231. Both objects were moved along the slit in an ABBA pattern.

The spectra were extracted in IRAF using standard procedures to trace the spectra on pairwise-subtracted images. We used Ar and Xe lamps to determine the wavelength scale, and cross correlated the individual spectra near the strong telluric absorption bands from $\lambda = 1.10$ to 1.15 μm to remove instrument flexure between exposures. Correction for telluric absorption was done with the same method as the IRTF spectra (Vacca et al. 2003).

In Fig. 2 we overlay the rescaled TIFKAM spectrum on the IRTF spectrum. The agreement between the two is excellent, with little change in the velocities or line depths over nearly 3 years. The depth of the strongest feature ($v = 4,500\,\mathrm{km^{-1}}$) is shallower in the TIFKAM spectra; this may be a consequence of a drop in continuum flux, as may be more prominent narrow He I*λ10830 emission line (§ 2.3).

There is an indication of the appearance of an absorption feature near $\lambda = 1.086\,\mu$m (observed wavelength ; rest wavelength $\lambda = 1.04216\,\mu$m) in the TIFKAM spectrum, which would correspond to a velocity of $v = 11,520\,\mathrm{km\,s^{-1}}$ if attributed to He I*λ10830. This feature may be marginally present in the IRTF spectrum. This feature cannot be a detector defect, as it is present in both the A and B spectra. There are no sky lines nor telluric features at this wavelength, nor any strong starburst galaxy absorption lines (e.g., Martins et al. 2013). Therefore, we tentatively conclude that a new, high velocity

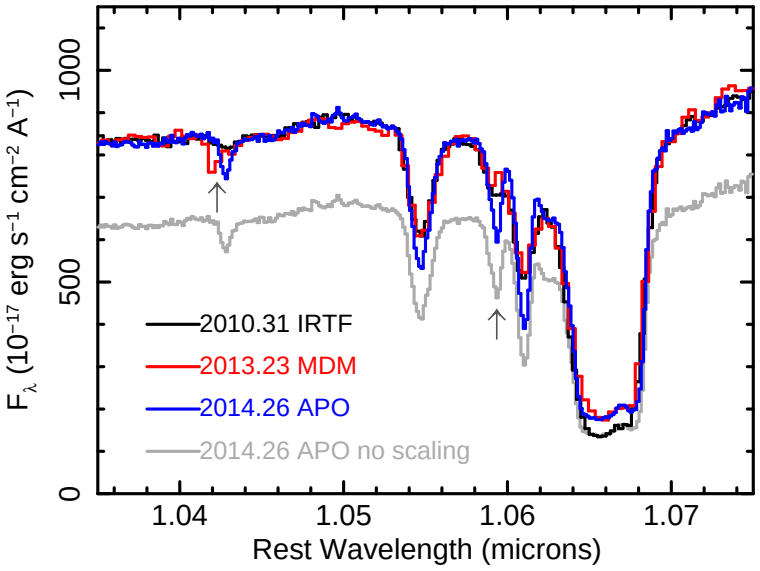

Fig. 2.— MDM TIFKAM (rescaled) and APO TripleSpec (both rescaled and with no scaling) spectra overlaid on the 2010 IRTF SpeX spectrum. The principal He I*λ10830 trough did not vary between the IRTF and APO observations, while the continuum flux decreased by about 24%. This is evidence that the trough is filled in by galaxy light. Tentative evidence for a new absorption component at $v \sim -11,520\,\mathrm{km\,s^{-1}}$ marked by the arrow in the MDM spectrum is confirmed in the APO spectrum, with possible deceleration to $v \sim -11,330\,\mathrm{km\,s^{-1}}$. Another component at $v \sim 6,620\,\mathrm{km\,s^{-1}}$ is observed only in the higher-resolution APO spectrum, and is apparently a consequence of the higher resolution.

absorption feature has appeared in Mrk 231, manifest at least in He I*λ10830.

2.3. APO TripleSpec Observation

To confirm the presence of the new high-velocity feature, Mrk 231 was observed on the night of 7 April 2014 using the TripleSpec infrared spectrograph (Wilson et al. 2004) on the 3.5-meter Astrophysical Research Consortium telescope at the Apache Point Observatory.

A total of 16 150-second exposures were made, moving the image along the slit in an ABBA pattern. The 1.″1 slit was used, yielding an effective resolution of $\sim 110\,\mathrm{km\,s^{-1}}$ (based on the widths of the arc lamp lines) in the vicinity of the He I* line. Ten 30-second observations of the A0 telluric standard star HD 116405 were made at similar airmass immediately following the quasar observation.

The spectra were extracted in a standard manner using TripleSpecTool, a modification of SpexTool (Cushing et al. 2004; Vacca et al. 2003). TripleSpecTool uses the airglow emission lines for wavelength calibration. To account for a very small amount of flexure, wavelength calibration solutions were computed for each pair of exposures. Telluric correction was performed using the same method as for the IRTF spectra (Vacca et al. 2003).

Fig. 2 shows the TripleSpec spectrum overlaid on the MDM and the IRTF spectra. The unscaled spectrum matches the IRTF spectrum in the bottom of the large trough, while the continuum level is about 24% lower. We interpret this as evidence that the central engine continuum flux level of the object has decreased over the four-year period between the observations, and that the trough is filled in by galaxy light, principally. The APO spectrum confirms the presence of the new high-velocity component tentatively detected in the MDM spectrum, although the velocity now appears to be lower, at $11,330\,\mathrm{km\,s^{-1}}$.

Fig. 2 also shows a component at $\sim 6,620\,\mathrm{km\,s^{-1}}$ that does not appear in either the IRTF or MDM observation. In addition, the absorption lines appear deeper in the APO observation. Both of these features appear to be a consequence of the higher resolution of the APO spectrum. We tested this idea by convolving the APO spectrum with a Gaussian kernel with a FWHM of $320\,\mathrm{km\,s^{-1}}$ (three bins), approximately the value necessary to degrade the APO $110\,\mathrm{km\,s^{-1}}$ resolution down to the IRTF $330\,\mathrm{km\,s^{-1}}$ resolution. When that is done, the new feature at $\sim 6,620\,\mathrm{km\,s^{-1}}$ disappears, and the lines become as shallow as

those in the other spectra. It is worth noting, however, that this $\sim 6,620\,\mathrm{km\,s^{-1}}$ component does not appear in the (Rupke et al. 2002) Na I profile (§ 4.3, Fig. 8) which has a higher velocity resolution of than the APO spectrum.

The high resolution and high signal-to-noise ratio of the APO data yielded an additional result. After aligning the spectral images in the dispersion direction, we created $A - B$ pairs and aligned the results in the spatial direction to create a single spectral trace. We then extracted profiles in the spatial direction and determined the amplitude and width of the profile as a function of wavelength (Fig. 3). The amplitude mirrors the spectrum, as it should. The width, however, varies. Away from the trough, the mean width of 3.81 pixels corresponds to a point spread function width of about 1.5 arcseconds. The profile within the trough is broader. This is most simply explained if the absorber completely covers the continuum source, and the trough is filled in by light from the partially-resolved host galaxy. The broadest part of the trough has a width of 4.66 pixels. Assuming that the PSFs add in quadrature, we infer that the resolved feature has an intrinsic width of 1.05 arcseconds, corresponding to 900 parsecs. An unexpected result of this analysis is that the longer wavelength portion of the trough is narrower than the shorter wavelength portion. In addition, the trough is not precisely flat on the bottom, but has slightly larger amplitude at longer wavelengths. This result is most simply explained if a small amount of AGN or unresolved galaxy leaks through the absorber. Based on the difference in amplitudes, that portion would corresponds to about $\sim 25\%$ of the galaxy light, and only $\sim 4\%$ of the unobscured AGN continuum.

2.4. KPNO Observation

Optical spectroscopic observations were performed during an observing run at Kitt Peak National Observatory using the Mayall 4-meter telescope on 2011 May 6. We used

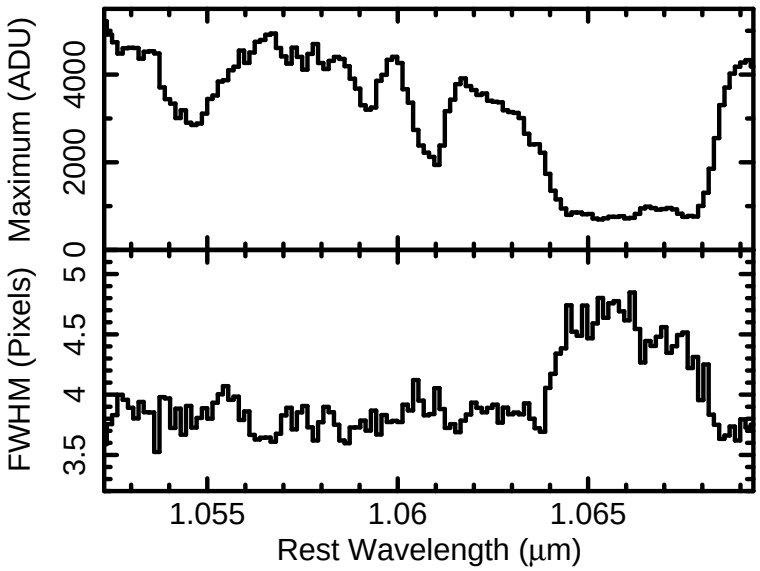

Fig. 3.— The results of measuring the profile in the spatial direction as a function of wavelength from the combined APO spectral images. The top panel shows the amplitude of the profile, which mirrors the extracted spectrum. The lower panel displays the FWHM of the profile. The profile is broader in the large trough, suggesting that the trough is filled in by light from the partially-resolved host galaxy.

the KPC–007 grism, which has a dispersion of 1.39Å per pixel, and resolution of 3.5Å. It is also one of the bluer gratings available, with good sensitivity up to the atmospheric cutoff. We observed Mrk 231 using a blue setting with a nominal wavelength coverage between $\sim$ 3200–6000Å. However, the sensitivity dropped steeply at the blue end due to the atmospheric cutoff, and at both ends due to vignetting. Measurement of arc lamp lines in the vicinity of the features of interest indicated a resolution of $170\,\mathrm{km\,s^{-1}}$.

Four 15-minute observations were made for a total exposure of 60 minutes at low airmass. Conditions were not photometric; however, the count rates from individual spectra deviated from the mean by only about 2.5% at the well-exposed central part of the

spectrum, increasing to $\sim$ 15–20% on the vignetted edges. We note that the He I* and Ca II absorption lines were covered in the well-exposed part of the spectrum. Standard reduction using IRAF was performed. The spectrum, corrected for Galactic reddening, is in shown Fig. 1.

The Na ID absorption line fell at the very red edge of the spectrum. Due to vignetting and differential refraction, we did not consider this part of the spectrum to be very reliable. However, one feature of the data was useful. Among the four spectra, the red-end flux decreased steadily with time as the red image of the object migrated out of the slit. However, the flux in the base of the Na ID absorption line remained constant. We take this as an indication that the continuum filling in the base of that line originates in the host galaxy, in particular in the nuclear starburst known to be present (e.g., Davies et al. 2004). This interpretation is consistent with the lack of polarization of this feature (e.g., Goodrich & Miller 1994; Smith et al. 1995; Gallagher et al. 2005). This will be discussed further in §4.3.

We measured the redshift using a very small and narrow Hβ line that lies on top of the broad Hβ. This feature most likely originates in the starburst, since narrow-line region emission in this object is essentially undetectable. The redshift inferred is 0.04215, which differs from the Veilleux et al. (2013) value by $\sim 15\,\mathrm{km\,s^{-1}}$, a negligible amount considering the resolution of the spectrum.

2.5. Supplementary Data

A principal goal of this paper is to investigate the spectral energy distribution from near-UV to 2.5 microns. Our KPNO spectrum only covers the blue optical portion, while our IRTF spectrum extends down to 8054Å in the rest frame, and so we needed to

obtain other data from the literature to span the gap. In addition, as discussed above, the well-known Na ID line falls at the edge of our KPNO spectrum, and is probably not very reliable. We therefore digitized the optical part of the spectrum shown in Fig. 3 in Veilleux et al. (2013); that spectrum was obtained at Keck in 2001. That figure did not adequately sample the Na ID line, so we digitized the absorption profile of the Na ID line shown in Fig. 11 of Rupke et al. (2002), and applied the inferred opacity profile to the continuum in the vicinity of the Na ID. These figures were plotted in the observed frame, and so we shift to the rest frame using $z = 0.0422$.

We also digitized the Mrk 231 "5kpc" spectrum shown in Fig. 3 in Rodríguez Zaurín et al. (2009); this nomenclature differentiated the spectrum from others reported in that paper that sample the outskirts of the host galaxy. This spectrum was taken on the ISIS dual-beam spectrograph on the 4.2m William Hershel Telescope. It has better coverage and signal-to-noise ratio at short wavelengths than does our KPNO spectrum, and even appears to show the Na I$\lambda\lambda$3302, 3303 absorption line corresponding to the principal BAL trough.

In addition, we wanted to use the *HST* FOS spectrum to constrain the continuum. Since our interest was in the shape of the continuum, rather than, e.g., detailed analysis of the absorption lines, we simply digitized the spectrum shown in Fig. 1 of Smith et al. (1995), and shifted to the rest frame using $z = 0.0422$.

2.6. Merging the Spectra

We next merged the five spectra (the KPNO spectrum, the IRTF spectrum and the three digitized spectra) in order to obtain a broad-band continuum. This procedure was hampered by the fact that slit losses make the ground-based spectra fluxes unreliable. At the same time, the *HST* observation was made in 1992, and therefore variability could affect

the relative fluxes of the spectra. But because the *HST* FOS aperture is large (3.7"× 1.3" effective size) and likely did not suffer any slit losses, we start with the *HST* spectrum and proceed toward longer wavelengths, scaling segments of spectra and joining them end to end.

The KPNO spectrum, Veilleux et al. (2013) spectrum, and the Rodríguez Zaurín et al. (2009) spectrum overlap over part of the optical band. Comparing these three spectra, we find that the shapes of the Veilleux et al. (2013) and Rodríguez Zaurín et al. (2009) spectra agree well overall. However, the Rodríguez Zaurín et al. (2009) spectrum displays an offset of the red and blue sides at $\sim$ 5180Å (rest frame) compared with both the Veilleux et al. (2013) and the KPNO spectrum. The Rodríguez Zaurín et al. (2009) spectrum was taken with a dual-beam spectrograph, and we speculate that this offset originates in calibration issues at the dichroic crossover. Avoiding the offset region, we use the Rodríguez Zaurín et al. (2009) spectrum at shorter wavelengths, switching to the Veilleux et al. (2013) for the necessary longer wavelength coverage.

The KPNO spectrum is slightly bluer than the Rodríguez Zaurín et al. (2009) spectrum ($\sim$ 15% brighter at $\sim$ 3600Å when the spectra are aligned at Hβ). This is possibly due to our spectrum including a larger fraction of the nuclear starburst, since the Balmer absorption lines appear deeper in our spectrum. So we do not use it for construction of the merged spectrum, although we use it for spectral fitting (§4.1).

Taking these considerations into account, we proceeded as follows. The *HST* spectrum overlaps with the Rodríguez Zaurín et al. (2009) spectrum near 3150Å, and we scaled and merged those two at this point. We then used the Rodríguez Zaurín et al. (2009) spectrum up to 4027Å, and scaled and merged the Veilleux et al. (2013) spectrum longward of that point. The Veilleux et al. (2013) spectrum extends to quite long wavelengths, with a $\sim 2,500$Å overlap with the IRTF spectrum, but the IRTF spectrum has better

signal-to-noise ratio to short wavelengths, so we used the scaled IRTF spectrum longward of 8223Å.

The merged spectrum is shown in Fig. 4. Overlaid on the merged spectra are Keck nuclear fluxes (obtained using interferometry Kishimoto et al. 2009) and *HST* (Kishimoto et al. 2007) fluxes obtained from NED. The long-wavelength infrared photometry agrees well with the results of the merging process, which started from short wavelengths. We took this convergence as evidence that our merged spectrum is reasonably representative of the true continuum spectrum.

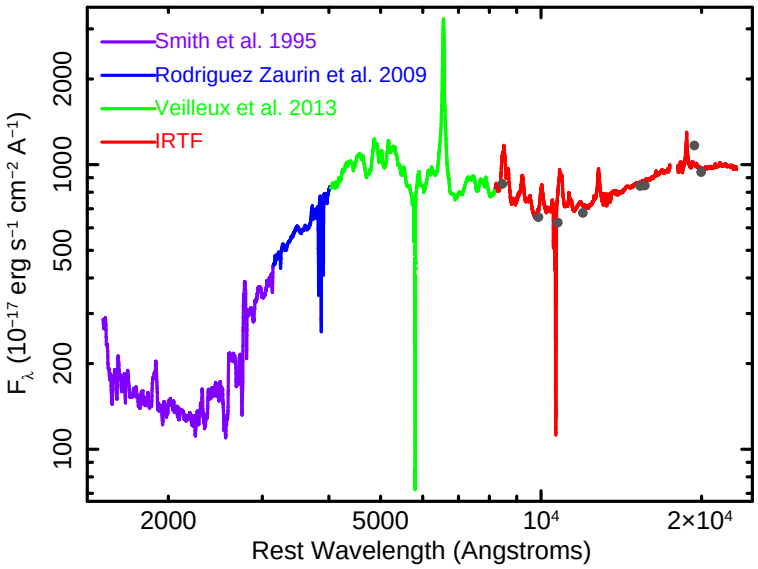

Fig. 4.— The broad band spectrum of Mrk 231, created through merging digitized spectra with the IRTF spectrum. The merging procedure started on the blue end with the *HST* spectrum, and proceeded segment by segment to long wavelengths (see §2.6 for details). The good agreement with the nuclear photometry points (gray solid circles) suggests that the flux calibration of the merged spectrum is reasonably accurate.

3. Reddening

The unusual shape of the near-UV to optical continuum has been noted previously by Smith et al. (1995) and Veilleux et al. (2013). As discussed by Veilleux et al. (2013), it is not consistent with any typical reddening curve. More specifically, the optical region of the spectrum is not particularly red; Boksenberg et al. (1977) suggest $A_V = 2.3$. However, the near UV drops dramatically, and Veilleux et al. (2013) show that the HST FOS quasar composite spectrum (Zheng et al. 1997), normalized at ~ 3600Å, must be reddened by a curve described by $A_V \sim 7$ mag to explain the steeply falling near-UV spectrum (Veilleux et al. 2013, see their Fig. 3). Note $A_V \sim 7$ is not, by itself, anomalous; for example, the radio galaxy Centaurus A is estimated to have $A_V \sim 14$ (Marconi et al. 2000). The property that is both unusual and difficult to explain with typical reddening curves is the apparently low reddening in the optical spectrum and the much higher reddening in the near UV. Anomalously steep reddening has been seen in several BALQSOs (Hall et al. 2002; Leighly et al. 2009; Jiang et al. 2013), but the mechanism for this reddening remains unexplained.

Previous discussions of the reddening have assumed foreground extinction in a screen with some standard ratio of total to selective extinction, say $R_V = A_V/E(B-V) \sim 3.1$ as in (e.g., Cardelli et al. 1988). Here, we offer an alternative explanation, namely that a reddening law like that invoked to explain unusually low values of R_V around Type Ia supernovae (Wang 2005; Goobar 2008), provides a good description of the optical and near-UV spectrum of Mrk 231.

The motivation and physics of circumstellar reddening is thoroughly discussed in Goobar (2008). For a spherical scattering medium with radius $R_{\rm CS}$ and mean free path $\lambda_{\rm eff} = 1/n\sigma_{\rm eff}$ (σ being a cross section), then the attenuation is well described by the typical screen case when $\lambda_{\rm eff}$ is much greater than $R_{\rm CS}$, similar to extinction by dust in the

interstellar medium. But when $\lambda_{\rm eff} \ll R_{\rm CS}$, corresponding to multiple scatterings, more blue photons will be removed from the line of sight, since these photons have longer path lengths for reasonable assumptions about wavelength-dependent scattering. A secondary effect is that the geometry allows photons to be added back into the line of sight. The radiative transfer appropriate for this case was developed by Witt et al. (1992); their Fig. 1 is particularly illuminating.

We use the empirical extinction parameterization derived by Goobar (2008), $A_\lambda/A_V = 1 - a + a(\lambda/\lambda_V)^p$ (Equation 3 in that paper), to explore whether a spherical geometry with significant optical depth can explain the unusual reddening in Mrk 231. We continue to refer to this model as "circumstellar reddening," even though here we are implicitly applying it on length scales appropriate for an active nucleus. We note that while the Goobar (2008) parameterization was developed from Monte Carlo simulations of light propagation for the U (i.e., 3600Å) through K photometric bands, we will extrapolate down to 2400Å in our analysis. Although it cannot be known whether or not the functional form will describe this region precisely, we expect that the power law dependence will describe the general trend, since scattering opacity generally increases toward the blue.

To apply the reddening correction, we first sampled the log flux in the merged spectrum at approximately evenly-spaced values in log wavelength. We avoided the strong Fe II emission when possible, and we also did not consider the continuum emission shortward of $\sim$ 2300Å, as it appears to be a separate component (e.g., Veilleux et al. 2013; Smith et al. 1995). For the intrinsic, unreddened continuum, we used the Richards et al. (2006) quasar composite spectral energy distribution, which provided good coverage over the bandpass of interest. This spectral energy distribution includes nuclear continuum and torus emission, but has the host galaxy emission removed. (Because Mrk 231 is so close, the spectroscopic slit excludes most of the host galaxy emission except for the nuclear starburst). We found

that we needed an additional blackbody in the near infrared (over and above the torus emission included in the Richards et al. (2006) continuum) to obtain an adequate fit. The temperature of this component is consistent with the 3–5μm hump often seen luminous quasars that originates in hot graphite dust at the inner edge of the torus (Deo et al. 2011). The variable parameters that we considered initially were those describing the reddening model (A_V and the parameters describing the scattering and absorption properties of the dust, a and p; see Goobar (2008) for details), the blackbody temperature, and the normalizations of the blackbody and the Richards continuum. The figure of merit that we used to evaluate the goodness of fit was defined as the sum of the absolute value of the differences between the logarithmically sampled flux points and the Richards et al. (2006) continuum. We obtained two fits, one with all parameters included in the fit, while the other with the values of a and p fixed at values appropriate for Milky Way dust (Goobar 2008). The best fitting parameters for these two fits are given in columns 2 and 3, respectively, in Table 2, and the best fit is plotted in Fig. 5. The fit is good overall; the deviations in the optical plausibly may be ascribed to blue continuum emission from the nuclear starburst, and strong Fe II emission.

The values of a and p obtained this fashion may be used to obtain an estimate of $R_V = 2.74$, which is indicative of dust like that in the Milky Way, in contrast with $R_V \approx 1.65$ for an LMC-like extinction law (Goobar 2008). It is worth noting that SMC dust, often used for BALQSOs (e.g., Gibson et al. 2009), was not parameterized for circumstellar reddening by Goobar (2008) because the shape of the extinction curve was not suitable for explaining anomalous supernovae colors. Our best fitting parameters are close to the Milky Way dust case; we tried the parameters provided by Goobar (2008) for LMC dust, and they resulted in a much poorer fit.

The effective A_V derived from the fit is 1.5–1.6. In §6, we will describe the results of

Table 2. Best Fitting Goobar (2008) Reddening Parameters

Parameter[a]	All Parameters Free	Milky Way Dust
A_V	1.54	1.60
a	0.78	0.9 (f[b])
p	−1.72	−1.5 (f[b])
Inferred R_V[c]	2.74	2.79
T_{bb}	1460	1460
BB Normalization	0.24	0.18
Continuum Normalization	0.85	0.87

[a]The first three parameters describe the extinction in the V band and the extinction shape parameters according to $A_\lambda/A_V = 1-a+a(\lambda/\lambda_V)^p$ (Goobar 2008).

[b]These parameters describing the shape of the reddening curve were measured by Goobar (2008) to be appropriate for Milky Way dust, and are fixed during the spectral fitting.

[c]Computed using Eq. 4 from Goobar (2008).

Cloudy photoionization modeling (Ferland et al. 2013) in which we use A_V as the stopping criterion. However, the *Cloudy* stopping criterion corresponds to slab-type reddening models, while the A_V derived here is reduced due to the continuum scattered into the line of sight. Therefore, we needed to derive an equivalent A_V(slab) from our A_V(CS). We did that using Fig. 1 in Witt et al. (1992), which displays relative intensities due to direct light, scattered light, and total light as a function of τ_V for a dusty galaxy model. Our best fit $A_V(\mathrm{CS}) = 1.54$ corresponds to an attenuation of 4.1, which corresponds to a $\tau_V(\mathrm{CS}) = 1.4$. From the figure, we found that for $\tau_V = 1.4$, the scattered light amounts to about 35% of the total. This implies that for the same amount of dust and a slab geometry, the transmitted light would have been 35% lower, so that $A_V(\mathrm{CS}) = 1.54$ corresponds to $A_V(\mathrm{slab}) \approx 2$.

Mrk 231 is an exceptionally highly polarized Seyfert galaxy; its polarization properties have been discussed by Smith et al. (1995), among others. The polarization increases towards shorter wavelengths from the optical to ~ 3000Å, peaking at $\sim 15\%$, and dropping toward longer wavelengths. The high polarization underlines Mrk 231's similarity with other BALQSOs (e.g., Ogle et al. 1999). Optical polarization increasing toward the blue, as is observed in some Seyfert 1 galaxies, can be attributed to dust or electron scattering combined with a reddened view of the direct continuum (e.g., Wills et al. 1992; Leighly et al. 1997). Our model for the reddening in Mrk 231 assumes implicitly a spherical scattering medium. Due to symmetry, a perfectly spherical scattering medium will produce no net polarization. Therefore it may appear that our model for the reddening is inconsistent with the relatively high polarization observed from this object. However, we note that we would not need a perfectly spherical scatterer and complete coverage to produce the reddening we see; a high covering fraction would be sufficient. Then, intrinsic continuum may emerge through gaps in the reddening medium and scatter towards us on e.g., dust or electrons at a larger radius than our reddening medium. If the gaps lie along lines to the continuum source that are perpendicular to our line of sight, such that the electron scattering angle

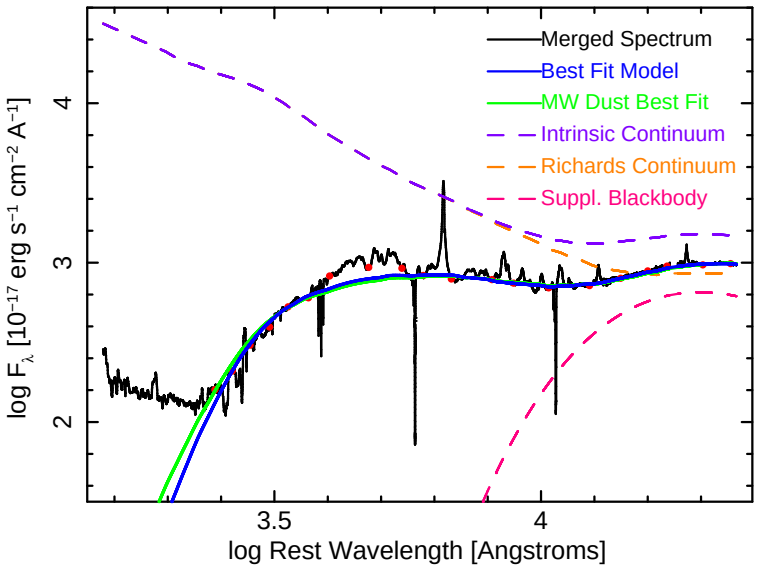

Fig. 5.— The merged spectrum overlaid with the best fitting circumstellar reddening model. The intrinsic continuum is assumed to be the composite quasar continuum, including the accretion disk and torus, derived by Richards et al. (2006). An additional black body with $T_{bb} = 1460\,\mathrm{K}$ is necessary. The circumstellar reddening is described by A_V and two shape parameters (Goobar 2008). The best fitting parameters are given in Table 2. The best-fitting reddening-shape parameters are close to that derived by Goobar (2008) for Milky Way dust; LMC-type dust does not fit as well.

approaches 90°, high intrinsic polarization will be produced. Combined with the strong reddening of the intrinsic continuum, significant net polarization increasing toward the blue would be observed.

Our success in modeling the unusual reddening from near UV through infrared with a modest value of $A_V(\mathrm{CS}) = 1.54$, corresponding to $A_V(\mathrm{slab}) \approx 2$, demonstrates the plausibility of much lower extinction values than derived by Veilleux et al. (2013). Furthermore, circumstellar reddening may be able to explain unusual reddening curves observed in some other quasars and AGN. One object that it may work for is IRAS 14026+4341 (Jiang et al. 2013), which shows steep reddening like Mrk 231, and has,

in addition, been reported to show Na I absorption, although it is much less strong than the absorption in Mrk 231 (Boroson & Meyers 1992). Jiang et al. (2013), however, show that the unusual reddening can alternatively be explained by an unusual dust-size distribution. Specifically, large grains are lacking, producing less reddening in the optical part of the spectrum. In either case, the interesting question may be: why does anomalous reddening occur in these two ULIRGs and not in other reddened quasars?

4. Absorption Lines

4.1. Accounting for the Nuclear Starburst Emission in the KPNO Spectrum

The KPNO spectrum shows Balmer absorption lines that are a clear indication of the presence of early-type stellar emission in the spectrum, most likely from the nuclear starburst. These have been noticed in the past (e.g., Boksenberg et al. 1977), but are rarely commented upon in more recent spectra. We speculate that this component is more prominent in our spectrum due to the use of a slightly large slit (1 arcsecond). In addition, as noted above, our KNPO spectrum appears bluer in the same bandpass than the spectrum presented by Rodríguez Zaurín et al. (2009), as it should if the quasar spectrum were contaminated by early-type stellar emission. Our goal is to extract the properties of the absorption lines that absorb the central engine emission but not that of the host galaxy. Therefore, we need to account for the host galaxy emission before we can measure the absorption line properties.

To prepare the KPNO spectrum for analysis, we first renormalized it to the merged spectrum at its long wavelength end, and then used the best-fitting effective reddening function derived in §3 to deredden it. We then fitted with a power law, Fe II pseudo-continuum, emission lines (principally Balmer lines), absorption lines, and a single-burst

galaxy template. We used the line catalog from Véron-Cetty et al. (2004), convolved with a gaussian of width $2000\,\mathrm{km\,s^{-1}}$ for the Fe II pseudo-continuum. The Balmer lines are somewhat broad, and higher order lines have such low contrast that they are difficult to measure independently of one another. Therefore, we constrained not only their width and separation, but also their relative intensities. We assumed that the Balmer line emission could be approximated by emission from a gas in partial local thermodynamic equilibrium (PLTE; Popović 2003), and therefore their ratios are characterized by a temperature. We found that the temperature is not tightly constrained, and $T = 5000\,\mathrm{K}$ works well. We included Balmer lines from Hβ to H9 at 3835Å. In addition, we needed an emission line that can probably be attributed to [O II]$\lambda\lambda 3726, 3729$ from the star formation (e.g., Ho 2005). We assume that the absorption lines absorb the nuclear emission (i.e, power law and emission lines), but not the starburst continuum.

We used GALAXEV, the library of evolutionary stellar population synthesis models computed with the isochrone synthesis code of Bruzual & Charlot (2003), for the single-burst galaxy template. Davies et al. (2004) estimated the age of the nuclear starburst to be between 10 and 100 Myr, and therefore we experimented with ready-made template spectra for 25, 100, and 290 Myr starbursts at $z = 0.05$. The principal difference among these spectra distinguishable in the fitted bandpass of the KPNO spectrum is their slope. That is, the 25 Myr template is the steepest, the 100 Myr is somewhat flatter, and the 290 Myr template is the flattest of the three. In the spectral fitting, the steepness of the galaxy spectrum is compensated by the power law. So, although the goodness of fit is comparable among the three choices, the 100 Myr template yielded a power law slope and normalization almost exactly the same as the Richards et al. (2006) spectrum (see Fig. 6). This supports our contention that the KPNO spectrum is steeper than the merged spectrum simply because of the additional 100 Myr starburst component. The best fitting model is shown in Fig. 6.

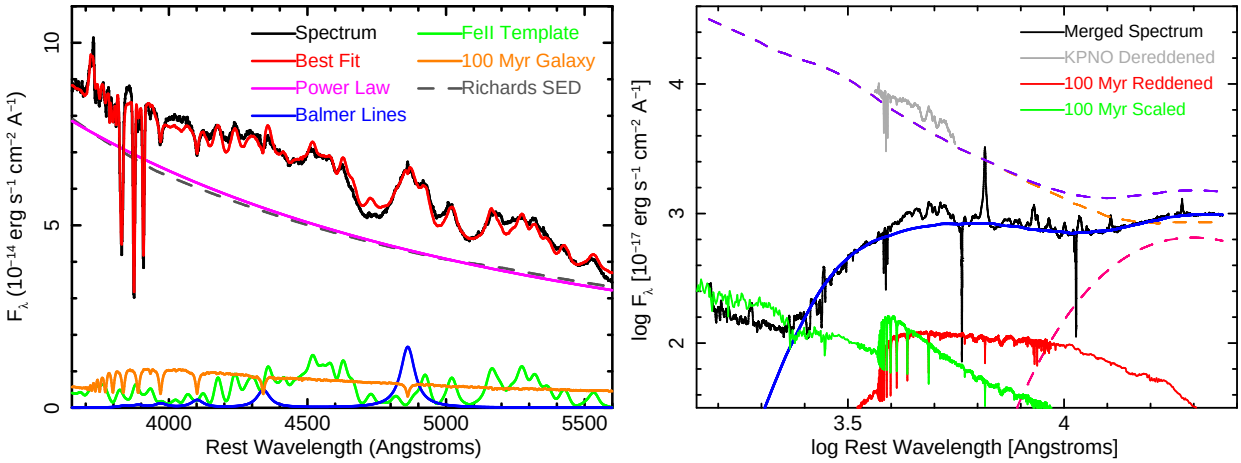

Fig. 6.— *Left:* The KPNO spectrum, corrected for reddening, includes light from the young nuclear starburst (e.g., Davies et al. 2004), modeled here using a 100 Myr single-burst galaxy spectrum. See §4.1 for a description of the other components. Modeling the galaxy spectrum allows us to determine the apparent optical depths of the absorption lines with respect to the nuclear continuum and broad-line region emission. *Right:* The galaxy component inferred from spectral fitting is shown in green. An unreddened galaxy SED scaled to the amplitude of the reddened one is shown in red. An unreddened galaxy component this bright would contribute unobserved stellar spectral features in the the far UV, and therefore we infer that the nuclear starburst is also reddened.

The young starburst component is likely to be the same one reported by Davies et al. (2004) from imaging analysis. They inferred the presence of a nuclear star-forming disk composed of young stars (10–100 Myr) with length scale 0.18"–0.24", corresponding to 150–200 pc. It is worth noting that the NUV spectrum was observed using FOS and the 4.3 aperture which subtends 3.7"×3.7"(effectively 3.7"×1.3" because it overfills the detector; Smith et al. 1995). Similarly, the UV spectrum was observed using COS with a 1.0 aperture, a circular aperture with a size of 0.86". In both cases, any light from the nuclear starburst would be included in the HST spectrum. As noted by Veilleux et al. (2013), there are no features originating in hot stars in the far UV spectrum, and therefore

it appears that the nuclear starburst is also attenuated by the circumstellar scattering. To investigate this point further, we show the inferred level of the galaxy component overlaid on the broad-band spectrum in Fig. 6. The dereddened KPNO spectrum is shown in light grey. Our dereddening of the KPNO spectrum implicitly assumes that the stellar component is reddened by the same amount as the AGN component. The reddened galaxy component, shown in green, was obtained using the stellar component normalization from the spectral fitting and applying the reddening. It is possible, however, that only the AGN component is reddened, and the galaxy component is unreddened. We can approximate this situation by normalizing the unreddened galaxy SED to the reddened one in the middle of the fitting band pass, shown in the figure in red. This unreddened spectrum, extrapolated to the near UV, would contribute stellar spectral features that are not observed. Therefore, the starburst is likely also reddened, although it may not be reddened by the same amount as the AGN component.

The Ca II$\lambda\lambda$3934, 3968 lines and He I*λ3889 were modeled using optical depth profiles that have a gaussian shape. We note that modeling the starburst component explicitly allowed us to detect additional quasar absorption lines attributable to higher velocity He I* appearing at 3786 and 3810 Angstroms (§4.3, Fig. 6). These features have been previously reported by Boroson et al. (1991).

4.2. Extracting the He I*λ10830 Absorption Profile

The IRTF spectrum is rather complicated. There is strong emission from Paschen lines, and the Ca II IR triplet emission is very strong and prominent. Evidence for the nuclear starburst is also present, including e.g., the CO 6-3 bandhead (Davies et al. 2004) and the narrow emission Fe II lines mentioned above. We limit detailed analysis and discussion to the region around He I*λ10830.

Again, we needed to estimate the starburst contribution. This was not easy; for example, BC03 spectra (Bruzual & Charlot 2003) that worked so well in the analysis of the KPNO spectrum have reduced spectral resolution longward of $\sim 1\,\mu$m. Maraston (2005) provides model spectra with sufficient resolution; however, those models appear to only have absorption lines, and lack the emission lines from the starburst that are important in the region of the spectrum around He I*. So, to estimate the starburst contribution, we used a near-IR template spectrum created from the spectra of star-forming galaxies (Martins et al. 2013) provided by L. Martins. This template was created by averaging the near-IR spectra of 23 low-luminosity starforming galaxies. Comparison of the template with the Mrk 231 spectrum revealed that various features, such as narrow line emission and small absorption features, were represented in both spectra. However, as discussed by Martins et al. (2013), the spectra of the sample galaxies vary significantly, with some objects showing brighter emission lines and others showing deeper absorption features. Since we don't know which type of starburst the NIR spectrum of the Mrk 231 starburst most closely resembles, the results from the use of this template must be considered representative rather than definitive.

We fitted the Mrk 231 spectrum with a model consisting of the starburst galaxy template, a power law, and four gaussians between 10290 and 11210Å, excluding regions around the absorption lines from the fitted bandpass. One gaussian was necessary to model Pγ, but two were required to model He I*λ10830 emission; the line apparently has a blue asymmetry. The bluer gaussian is offset from the red one by about $1,600\,\mathrm{km\,s^{-1}}$, and the asymmetry may be an indication of an outflow. Alternatively, it could be blended emission from another, unidentified line, such as has been found in PDS 456 (Landt et al. 2008). We also included an emission line at 10498Å that may be attributed to a blend of Fe IIλ10491, 10502. The best fit is shown in Fig. 7. It is interesting to see how the template (which was free to vary in normalization) nearly accounts for the continuum

under the He I*λ10830; it represents $\sim$ 12% of the total. However, the normalization of the template in the spectral fit is most likely being driven principally, although not wholly, by the amplitude of the narrow He I*λ10830 and Pγ emission from the starburst. It is therefore not very well constrained; the error was 9% of the normalization for the starburst template, versus 2% for the power law normalization. It is worth noting that similar relative normalizations were obtained by fitting broad-line-free segments of the spectrum to a powerlaw plus the template.

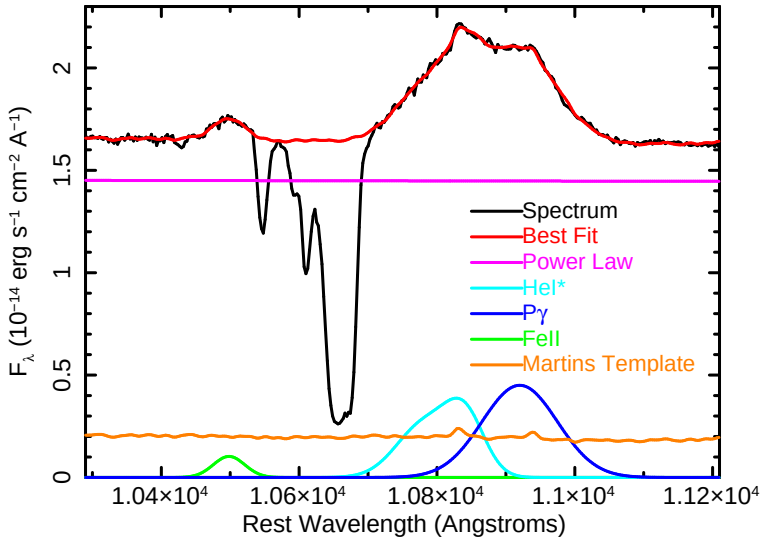

Fig. 7.— The section of the IRTF spectrum including the He I*λ10830 absorption line. The spectrum was modeled, as discussed in §4.2, using a power-law continuum, emission lines, and a starburst template (Martins et al. 2013). Including the galaxy spectrum explicitly in the model allows us to determine the apparent optical depth of the He I*λ10830 absorption line with respect to the nuclear continuum and broad-line region emission.

4.3. Absorption Line Profiles

Using the results of the spectral fitting described in §4.1 and §4.2, we display the He I*λ3889, He I*λ10830 and Ca II profiles in Fig. 8. As noted above, our Na ID line falls off the edge of the detector, so here we plot the digitized profile from Rupke et al. (2002). Their spectrum had better spectral resolution than ours ($65\,\mathrm{km\,s^{-1}}$), revealing enhanced structure in the profile. Also, Na ID is a doublet, with rest-frame wavelengths of 5889.95 and 5895.92Å, and effective separation of $\sim 300\,\mathrm{km\,s^{-1}}$. We derive an approximate velocity profile for a single component by joining the left side of the profile, dominated by Na Iλ5890 to the right side, dominated by Na Iλ5896. The true single component profile would be somewhat narrower than the approximation.

The Na ID profile has two principal components, including a large one near $-4,500\,\mathrm{km\,s^{-1}}$, and a second one near $-6,100\,\mathrm{km\,s^{-1}}$. A third component is sometimes seen in this line near $-8,000\,\mathrm{km\,s^{-1}}$ (e.g., Boroson et al. 1991; Kollatschny et al. 1992; Forster et al. 1995). Rupke et al. (2002) find some evidence for this component, but it is very weak. In contrast, the two higher-velocity components (at $-6,100$ and $-8,000\,\mathrm{km\,s^{-1}}$) appear stronger and more prominent in He I*λ10830.

Both the Na I and He Iλ10830 lower-velocity components have essentially flat bottoms, a classic signature of saturation. The origin of the fill-in is debatable, but it quite possibly originates in the nuclear starburst. Another piece of evidence supporting this idea is the fact that while in other BALQSOs, where the flux in the absorption troughs is more polarized than the continuum (as would be the case with scattered light, Ogle et al. 1999), the polarized flux in the Na I trough is very low, essentially zero (e.g., Goodrich & Miller 1994; Smith et al. 1995; Gallagher et al. 2005). The level of the fill-in is slightly different in Na ID and He Iλ10830; that could be real, but could also be due to different amounts of nuclear starburst light in the aperture. Note that we subtracted starburst emission from

the He I*λ10830 spectrum (§4.2).

Possibly the most interesting feature is the differences in velocities observed between the high ionization lines, represented by He I*λ3889 and He I*λ10830, and the low ionization lines, represented by Ca II and Na I. For example, the He I*λ3889 line has a $\sim 75\,\mathrm{km\,s^{-1}}$ higher-velocity centroid than the Ca II lines. Furthermore, it is broader; the best fit width for the He I*λ3889 is $790\,\mathrm{km\,s^{-1}}$, while the best fit width of the Ca II lines is $490\,\mathrm{km\,s^{-1}}$. Turning to the saturated lines, the FWHM points for the principal He I*λ10830 absorption lines are -5434 and , $-4080\,\mathrm{km\,s^{-1}}$, while for Na I, the values are -5144 and $-4080\,\mathrm{km\,s^{-1}}$. So while the red-edge velocities line up, the blue edges differ by $\sim 290\,\mathrm{km\,s^{-1}}$. Thus, while the profiles of all the lines discussed in this paper are similar enough to have been produced in roughly the same kinematic component, the He I*-absorbing gas is moving faster than the Ca II and Na I absorbing gas. We will discuss the implications of this fact on the *Cloudy* modeling in §6, and speculate on the physical conditions leading to this result in §6.2.

For the *Cloudy* modeling, we need measurements and limits of the ionic column densities. Note that we will limit the photoionization analysis to the principal absorption feature centered near $-4,500\,\mathrm{km\,s^{-1}}$. For He I*$\lambda$3889, the Ca II lines, and He I*λ10830, we used the fitted gaussian absorption lines to measure the apparent optical depths. We then integrated over the absorption profiles to obtain the ionic column densities (Savage & Sembach 1991). The results are given in Table 4.3. Our measurement of log column He I*λ3889 of 15.0 is slightly smaller than the one obtained by Rupke et al. (2002) of 15.3. This appears to be partially a consequence of their curve of growth analysis method; when we integrate over a digitized version of their profile, we obtain 15.17. Likewise, our measurement of the Ca IIλ3934 log column of 14.0 is somewhat lower than theirs (14.4), possibly for the same reason. Alternatively, absorption profile depth variability or galaxy subtraction uncertainties may account for the differences.

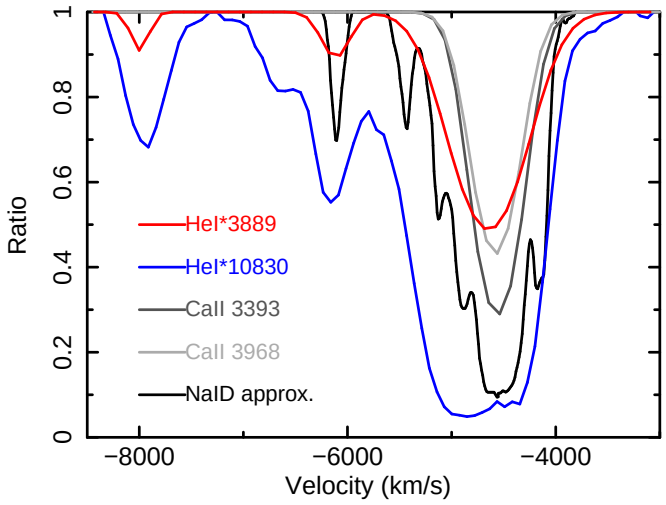

Fig. 8.— Velocity profiles for the optical and infrared absorption line complexes investigated in this paper. All lines were measured from our KPNO and IRTF spectra, excluding the starburst component (§4.1, §4.2), except for Na ID, which was taken from Rupke et al. (2002), and the approximate profile for a single component extracted as described in §4.3. Their spectrum has higher resolution ($\sim 65\,\mathrm{km\,s^{-1}}$) than ours (KPNO: 170 km s; IRTF: $330\,\mathrm{km\,s^{-1}}$), and the additional structure in that profile is an effect of differing resolution rather than a physical difference. All absorption lines have a similar velocity dependence; however, the He I* lines, produced in the H II part of the outflow, are characterized by higher velocities than the Na I or Ca II lines, produced in the partially-ionized and neutral part of the outflow.

Several of these measurements merit further comment. The Ca II lines are a doublet with a ratio of the product of oscillator strength f_{ik} and wavelength λ of ~ 2. However, the measured optical depth ratio is 1.48. This is a classic manifestation of partial covering, and therefore the column densities measured by integrating over the apparent optical depths will yield only lower limits on the column density. Since we have measurements for both lines, we use the formalism given by Sabra & Hamann (2005), Equations 5 and 6, estimating the Ca^+ covering fraction and true column density to be 0.76 and $2.0 \times 10^{14}\,\mathrm{cm^{-2}}$, respectively.

Table 2. Ion Column Densities and Limits for the Principal Absorption Component

Line	log Column Density	Comment
He I*λ3889	14.96	measurement
Ca IIλ3934	13.96	lower limit
Ca IIλ3968	14.01	lower limit
Ca II	14.2	accounting for partial covering
Na I	14.5	Rupke et al. (2002)
He I*λ10830	14.3	lower limit
H I in $n = 2$	12.3	upper limit

Rupke et al. (2002) estimate a similar column density, and velocity-dependent covering fraction between ~ 0.7 and 0.85.

The flat bottom of the He I*λ10830 profile suggests that it is saturated; the estimate of the lower limit on the He I* column density obtained from this line is given in Table 4.3. For *Cloudy* modeling, we use the column density measured from the apparently unsaturated He I* at 3889Å. Integrating over the line yielded a log column density of 14.96. Rudy et al. (1985) estimated a similar value of $1 \times 10^{15}\,\mathrm{cm}^{-2}$. We do not think that partial covering is significant for this line, for the following reasons. As discussed above, the He I*λ10830 absorption line has a flat bottom and is plausibly filled in by stellar continuum. If that is true, then the gas containing metastable helium completely covers the photoionizing continuum source. Since He I*λ3889 does not appear to be saturated, and the gas containing metastable helium completely covers the source, and because our spectral fitting accounts for the stellar component (§4.1), then integrating over the line yields a measurement of the true metastable helium column density rather than a lower limit.

As discussed above, Na I falls off the end of our bandpass, and so we use the column

density estimated by Rupke et al. (2002) of $3.1 \times 10^{14}\,\mathrm{cm}^{-2}$.

Finally, it is useful to estimate an upper limit on hydrogen column density in $n = 2$ from the lack of Balmer line absorption. To do this, we shifted the Ca IIλ3933 optical depth profile to the Hβ wavelength, and increased the optical depth until the absorption line appeared below the spectrum minus the uncertainty. We then computed the corresponding Balmer column density. Absorption from $2s$ has a different oscillator strength ($f_{ik} = 0.103$) than absorption from $2p$ ($f_{ik} = 0.25$). Simulations show that both states should be present in the gas but the proportions vary. Previously, we have tuned the constraint to the proportions in the simulation (Leighly et al. 2011), but here we assume, for a rough estimate, that the representative oscillator strength is the mean of the two values ($f_{ik} \approx 0.177$). This yielded an upper limit for the hydrogen column density in $n = 2$ of $8.58 \times 10^{12}\,\mathrm{cm}^{-2}$. However, if we had had high signal-to-noise ratio spectra of the Hα region, we would have obtained a factor of ~ 4.4 times tighter constraint due to the larger values of λf_{ik} of Hα. Since Balmer absorption lines from the BALs have never been reported in this well-studied object, we use an upper limit of log hydrogen column density in $n = 2$ of 12.3.

5. Mrk 231's Physical Parameters

Using measurements obtained from the spectra and de-reddened SED, we can compute various physical parameters for the quasar in Mrk 231. These will be needed for discussion of physical scales. It has been recently shown by Landt et al. (2013) that the Paschen lines plus the 1-micron luminosity density can be used to obtain a single-epoch black hole mass estimate. The broad line FWHM is required for this estimate. The Mrk 231 Pα line shows an inflection, allowing the narrow component originating in the starburst to be modeled out. We obtained two estimates of the broad Pα line FWHM that yielded consistent results. The first value, $2770\,\mathrm{km\,s}^{-1}$, was obtained from a three-gaussian model of the Pα line

with the narrow component removed. The second value, $2805\,\mathrm{km\,s^{-1}}$, was obtained from a two-gaussian plus starburst fit, with the starburst removed. The 1-micron luminosity, λL_λ, was measured to be $5.5 \times 10^{44}\,\mathrm{erg\,s^{-1}}$ from the reddening-corrected intrinsic continuum shown in Fig. 5. The black hole mass estimates from the two FWHM values were the same to two significant figures, so we use the value $M_{BH} = 2.3 \times 10^8\,\mathrm{M_\odot}$. For this value of the black hole mass, the Eddington luminosity is $L_{Edd} = 2.88 \times 10^{46}\,\mathrm{erg\,s^{-1}}$.

We obtained the estimate of the bolometric luminosity in two ways. First, we normalized the continuum we use for *Cloudy* modeling (see §6) to the intrinsic 2500Å flux inferred from the dereddened intrinsic spectrum shown in Fig. 5, and then integrated over the continuum between $3.9 \times 10^{11}\,\mathrm{Hz}$ to $9.6 \times 10^4\,\mathrm{keV}$. The estimated bolometric luminosity was $8.35 \times 10^{45}\,\mathrm{erg\,s^{-1}}$. The second was obtained using the intrinsic 5100Å flux inferred from the dereddened intrinsic spectrum shown in Fig. 5, and then applying a bolometric correction of 10.3 (Richards et al. 2006). That estimated value of the bolometric luminosity was $7.86 \times 10^{45}\,\mathrm{erg\,s^{-1}}$. These estimates are very close to one another, and we use the mean value $8.1 \times 10^{45}\,\mathrm{erg\,s^{-1}}$ henceforth. For this value of the bolometric luminosity, the quasar component of Mrk 231 appears to be radiating at 28% of the Eddington luminosity.

Tacconi et al. (2002) obtain a much smaller value of the black hole mass in Mrk 231 of $1.3 \times 10^7\,\mathrm{M_\odot}$, based on the stellar dynamics, which implies a super-Eddington accretion rate. Davies et al. (2004) reconsidered this result, finding that the nuclear starburst complicates the measurement of the dynamical mass, and that the stars have a disk-like rather than a spherical distribution, which biases the dynamical mass estimate toward lower values. Davies et al. (2004) conclude that the dynamical black hole mass is actually $6 \times 10^8\,\mathrm{M_\odot}$, just a factor of 2.6 times larger than our estimate based on the Paschen line width.

Finally, we needed an estimate of the size of the 1 micron continuum-emitting region. The He I*λ10830 absorption line is deep enough that we could be certain that it covers

both the nuclear continuum emission and the torus emission. The torus will be larger, and a conservative estimate of the radius of the torus contributing to the 1.083 micron continuum is $R_{\tau K}$, the reverberation mapping radius of K-band photometry. $R_{\tau K}$ is given by Kishimoto et al. (2011) as $R_{\tau K} = 0.47(6\nu L_\nu(5500\text{Å})/10^{46}\,\mathrm{erg\,s^{-1}})^{1/2}\,\mathrm{pc}$, where the scaled optical luminosity $6\nu L\nu(5500\text{Å})$ is used for the UV luminosity. We estimated $\nu L_\nu(5500\text{Å})$ from the intrinsic continuum shown in Fig. 5, and found that $R_{\tau K} = 0.31\,\mathrm{pc}$.

6. Photoionization Modeling

6.1. General Constraints

Mrk 231 presents a significant challenge for photoionization modeling, even using just the few lines accessible in the optical and infrared spectra, as noted previously by Veilleux et al. (2013) and others. The fact that the lines have quite similar profiles, modulo saturation, suggests that they are all produced in gas with common kinematics, and therefore it is reasonable to assume that it is all part of a single physical construct. Furthermore, while the saturated lines are not black, their flat bottoms and the results of our analysis presented in §4.1 and §4.2 suggests that the fill-in principally arises in the nuclear starburst. Thus, the absorbing gas essentially fully covers the continuum emission region.

As noted in the introduction, the most remarkable feature of the Mrk 231 spectrum is the strong Na ID line. This line, from neutral sodium, is common in the ISM, but rather rare in quasars. The ionization potential of neutral sodium is only 5.14 eV; it is thus easily destroyed by the hard AGN continuum, and therefore it can only exist where it is shielded from the quasar continuum by other gas that contains the hydrogen ionization front (e.g., see also, Veilleux et al. 2013).

In contrast, He I* behaves as a high-ionization line. As discussed in Leighly et al. (2011) and elsewhere, He I* is the absorption from the $2s$ metastable state of neutral helium. That state lies 19.8 eV above the ground state; it cannot be populated by collisions, but rather is populated by recombination of He^+. This means that a photon with energy at least 24.6 eV is required to form He^+, which in turn implies that He I* is found in the H II region of quasars, along with other high ionization lines such as C IV. Furthermore, in gas illuminated by typically hard quasar continua, the neutral helium ionization front is coincident with hydrogen ionization front, and therefore the He I* absorption occurs in physically disjoint gas from the Na I absorption. This fact is independent of ionization parameter and density of the illuminated gas, and is simply a consequence of the fact that the 24.3 eV photon required to form He I* would easily destroy neutral sodium. Therefore, the least we can say is that the gas in which the He I* lines are formed is interior (i.e., closer to the photoionizing source) to the gas producing the Na I lines.

The second unusual and constraining property involves the fact that the velocity for He I* is slightly larger than that of Na I and Ca II. This fact by itself is not unusual; high-ionization lines often have higher velocities than low-ionization lines (e.g., Voit et al. 1993). However, in those cases, there are also usually differences in profiles and evidence for partial covering, so that, e.g., the low ionization lines could be produced in dense cores with relatively low velocity, while the high ionization lines are produced in a thinner wind possibly ablated from the cores and accelerated. For Mrk 231, the similarity of the profiles and the evidence for full covering, specifically for the He I*λ10830 and Na ID lines, implies that the same gas is responsible for both sets of lines. Other full-covering situations that might be similar would be, e.g., stellar winds and supernovae. However, in those cases, the flow is homologous, that is, $v \propto r$. This is opposite of the situation for Mrk 231, where the gas at a smaller radius (absorbing in He I*) is moving faster than the gas at a larger radius (absorbing in Na I and Ca II). This physical situation suggests perhaps that a shock would

be produced at the interface.

All of these facts imply that the absorption lines in Mrk 231 are sufficiently different from other BALQSOs that we cannot take the standard analysis approach, i.e., running a grid of models, varying density, ionization parameter, and column density, as well as metallicity and spectral energy distribution, and then determining the location in parameter space that best fits the absorption lines. Our approach is instead suggested by the physical picture laid out in the next section.

6.2. A Physical Picture and Cloudy Simulation Setup

Mrk 231 has a well-known nuclear starburst. Detailed analysis by Davies et al. (2004) reveal that the nuclear starburst has a disky configuration with length scale of 150–200 pc and an age of 10–100 Myr. Our analysis in §3 shows that the quasar continuum suffers extinction in a shell of dust that subtends a large solid angle. We suggest that the nuclear starburst produces the dust performing the scattering, and that the nuclear starburst may also be the origin of the gas in which the Na ID and Ca II absorption is occurring. However, a starburst would produce, by itself, very modest outflow velocities (hundreds of $\mathrm{km\,s^{-1}}$; e.g., Rupke et al. 2005). So we suggest that the acceleration originates from a a continuous quasar outflow impacting upon and accelerating, over time, the gas being processed by the starburst. The quasar outflow is the origin of the He I* absorption, while the accelerated processed gas is the origin of the Na I and Ca II absorption. This scenario can explain why the He I* lines have higher velocity than the low-ionization lines.

We note that quasar feedback, thought to be necessary to shut down star formation during the co-evolution of black holes and quasars, posits an interaction between quasar outflows and surrounding star-forming gas. It therefore may be that we are observing an

example of feedback in action.

This scenario also motivates what we have found by experimentation to be a key requirement in the photoionization model: a density increase between the H II region, where the He I* absorption occurs, and the partially-ionized zone, where the Ca II and Na ID lines are formed. This is because not only does Mrk 231 show strong He I* absorption, but the inferred column density of this line is quite large. As discussed in Leighly et al. (2011), a high column of metastable helium requires a high column of He^+. A large column density of He^+ is attained by a relatively high ionization parameter. In contrast, neutral sodium favors a low ionization parameter. Those two conditions can be met in the same slab of gas if there is an increase in density between H II region and the partially-ionized zone. Further, we assert that without the density gradient, Mrk 231 perhaps would resemble other FeLoBALs, similar to e.g., FBQS 1151+3822 (Lucy et al. 2014), with He I*, magnesium and Fe II lines, but no very low ionization lines like Ca II or Na I.

Physically, the density gradient or step could result from the BAL outflow impacting the starburst-processed gas, scooping it up and accelerating it. Perhaps something like the cloud-crushing scenario proposed by Faucher-Giguère et al. (2012), in which shocked gas cools, could be operating, with the difference that a large covering fraction should be produced. In principle, a dynamical model for the envisioned scenario could be constructed; however, that is beyond the scope of this paper, and it is not clear that such a model could be constrained usefully with the small number of lines measured.

Instead, we present a simple (i.e., toy) model to see if we can produce the column densities and limits that we measure, and explore the conditions required. We start with an assumption of constant pressure to produce the density gradient. We also assume solar abundances. While Mrk 231 appears to have an X-ray weak spectral energy distribution (Teng et al. 2014), we start with a typical quasar SED in order to examine the influence of

this parameter, and investigate an X-ray weak SED in §7.4. If the absorption is occurring in the starburst, dust is probably present in the gas. The analysis presented in §3 shows that, at least in the line of sight, the extinction is relatively modest, with $A_V(slab) \sim 2$. Therefore, we use, in our simulations, $A_V = 2$ as a stopping criterion. Two other parameters describing the gas are important: the dust-to-gas ratio and the depletion of various elements from the gas phase into dust.

§6.3 describes the *Cloudy* simulations and results for this simple model. The results are suggestive, but some aspects would be difficult to explain physically. §7 then describes the results of modifying the simple model assumptions one by one. Finally, §8 describes the results for a optimizing all of the parameters described in §7.

6.3. Simulations and Analysis

We used *Cloudy 13.02* (Ferland et al. 1998, 2013). For the initial spectral energy distribution, we used the so-called *Cloudy* AGN continuum with the same parameters as used by Korista et al. (1997)[5]. Default *Cloudy* solar photospheric abundances, taken from various sources described in the *Hazy* manual included with the *Cloudy* distribution, were used. We then modified those abundances using the approximate depletion scheme described below. Given that the reddening inferred in §3 was best described by Milky Way dust, we chose the *Cloudy* built-in ISM dust (Draine & Li 2007), and as noted above, used $A_V = 2$ as our stopping criterion. That is, the gas slab thickness was truncated by the software when $A_V = 2$.

[5]The *Cloudy* command for this continuum is "AGN Kirk". The model consists of a powerlaw with a slope of $\alpha_{uv} = -0.5$, an high energy exponential cutoff with $\log T = 6$, an X-ray power law with a slope $\alpha_x = -1.0$, and $\alpha_{ox} = -1.4$

The Milky Way galaxy is characterized approximately by a constant dust-to-gas ratio. But in the chaotic environment of a quasar, a Milky Way dust-to-gas ratio can not be guaranteed. Therefore, dust-to-gas ratio was included as a parameter, where, for example, a parameter value of 0.1 means that the dust-to-gas ratio was 10% of that in the ISM.

If dust is present, then some elements should be depleted onto the dust grains. It may be expected that the dust-to-gas ratio and the depletion should be coupled parameters; the larger the dust-to-gas ratio, the more metals should be removed from the gas phase. But they can be approximately independent if the dust is clumpy. In that case, significant metals can be removed from the gas by depletion onto dust, but if those dust clumps are larger than the relevant wavelengths, they may provide little reddening. We started with *Cloudy*'s built in depletion scheme[6]; for example, it predicts, for a standard dust-to-gas ratio, that calcium should be depleted by a factor of 10^{-4}, and sodium should be depleted by a factor of 0.2. We then defined a depletion parameter that ranged between zero and 1, and gives the logarithmic fraction of the depletion. Specifically, the standard calcium depletion by a factor of 10^{-4} would be assigned an abundance parameter equal to 1, while an abundance parameter of 0.5 would correspond to a depletion by a factor of 10^{-2}. This is simply a parameterization and there is no physical basis behind it. But given the uncertainty of dust depletion factors, especially potentially occurring in the AGN/starburst environment of Mrk 231, it served our purpose.

We explored ionization parameters between $\log U = -1.5$ and $\log U = 0.5$. We used a constant pressure to produce the density gradient, and specified the hydrogen density $\log n$ at the illuminated side of the slab. We explored values between $\log n = 3$ and $\log n = 5.5$ [cm^{-3}]. Thus our simulation grid was described by four parameters: the

[6]The full depletion scheme is given on page 77 of the *Cloudy* 13.02 manual *Hazy* and references therein.

ionization parameter $\log U$, the density $\log n$, the dust-to-gas ratio parameter, and the depletion parameter.

The simulations produced predicted column densities of the key ions: neutral sodium, metastable neutral helium, Ca^+, and hydrogen in $n = 2$. The simulation column densities were compared with the measured values given in Table 4.3 using a modified figure of merit ($MFOM$). Previously, we have used a figure of merit defined as the sum of the absolute value of the difference between the measured log column density and the simulation results weighted by the measurement uncertainties (e.g., Leighly 2004; Casebeer et al. 2006; Lucy et al. 2014). We have found that this figure of merit performs better than χ^2 in the face of outliers, although it is not easy to interpret statistically. Here, however, we needed to combine limits with measurements with error bars. Therefore, we used a modified figure of merit (MFOM) defined as before, except that we assigned a contribution to the sum equal to zero for an ion if either falls within the range defined by the measurement uncertainties, or is consistent with the upper or lower limit as appropriate for that ion. Therefore, any simulation which yielded an $MFOM$ equal to zero has all four column densities in agreement with the measurements and the limits.

We used a lower limit on neutral sodium of 14.5, a lower limit on He I* of 14.8, an upper limit on hydrogen in $n = 2$ of 12.5, and bounds on Ca^+ between 14.1 and 14.3. The sodium and hydrogen limits are the same as in Table 4.3, but our choices for He I* and Ca^+ require some explanation. First, we consider He I* a lower limit, given that we were not able to solve for partial covering for this line, although based on the discussion above, we think that the covering fraction is nearly 100%. Our best measured value for He I* is 14.96, and, in principle, that should be the lower limit. However, we relaxed that the limit to $\log N_{HeI*} > 14.8$, because of a limitation in the *Cloudy* modeling software. Physically, the H II region of the absorbing gas may be dust free if it is a wind that originates from

the quasar (see §6.2). However, *Cloudy* cannot accommodate a dust-to-gas ratio that varies through the slab. As will be discussed below, the dust unavoidably included in the simulation in the H II region suppresses production of metastable helium, and therefore, the He I* column produced by the simulation would be higher if dust were not present in the H II region. Furthermore, based on previous studies of He I* in the FeLoBAL quasar FBQS J1151+3822 (Leighly et al. 2011; Lucy et al. 2014), we know that we can attain column densities of metastable helium in the H II region for these values of ionization parameter, if dust were not present. Second, although we have a good measurement of the Ca^+ column of 14.2 including partial covering analysis (§4), the measurement is uncertain due to possible systematic errors and model dependencies; for example, the depth of the Ca II lines in the KPNO spectrum depends on the fractional contribution of the starburst, which, in our spectral fitting, depended on the age of the assumed starburst spectrum, and that was degenerate with the power law slope. Therefore, we assigned $MFOM = 0$ when the Ca^+ value lay between 14.1 and 14.3.

Since there are multiple points in parameter space where $MFOM = 0$, we did not assign a best fit based on the value of $MFOM$. Instead, we identified a characteristic solution defined by the $MFOM = 0$ grid point that lay at the minimum of the sum of the differences between each $MFOM = 0$ solution and every other one, normalized by the grid spacing. For this toy model, the characteristic solution turns out to be $\log U = -0.5$, $\log n = 3.75$, dust-to-gas ratio parameter equal to 0.075, and depletion parameter equal to 0.6. Fig. 9 shows contours of $MFOM$ in terms of our four parameters, orthogonal to this point. The parameter values where $MFOM = 0$ are marked. Table 3 gives the ranges and the values for the characteristic solution, which will be discussed in detail in §6.6.

Table 3. *Cloudy* Modeling Results

Parameter	Constant Pressure		Density Jump = 0.6[a]		Density Jump = 1.4[a]	
	Range[b]	Characteristic Solution[c]	Range[b]	Characteristic Solution[c]	Range[b]	Characteristic Solution[c]
			Simulation Parameters			
$\log U$[d]	−1.25 – 0.5	−0.5	−1.25 – 0.75	−0.25	−1.5 – 0.75	−0.5
$\log n$ [cm^{-3}][e]	3.0 – 4.75	3.75	3.0 – 5.5	4.25	3.0 – 5.5	3.75
Dust-to-Gas Ratio Parameter[f]	0.05 – 0.1	0.075	0.05 – 0.175	0.075	0.05 – 0.3	0.125
Abundance Parameter[g]	0.5 – 0.65	0.6	0.45 – 0.55	0.5	0.4 – 0.6	0.5
			Column Densities [cm^{-2}]			
log Total Hydrogen Column	22.6 – 22.9	22.7	22.3 – 22.9	22.7	22.1 – 22.9	22.5
log H II Region Column	21.6 – 22.2	21.9	21.1 – 21.8	21.3	21.1 – 22.0	21.7
log H I Region Column	22.4 – 22.8	22.6	22.3 – 22.9	22.7	22.0 – 22.9	22.4
Na I	14.5 – 15.1	14.85	14.5 – 14.9	14.6	14.5 – 15.2	14.6
He I*	14.8 – 14.9	14.83	14.8 – 15.3	15.0	14.8 – 15.4	15.2
Ca II	14.1 – 14.3	14.14	14.1 – 14.3	14.3	14.1 – 14.3	14.2
H I n=2	11.8 – 12.3	11.95	10.6 – 12.3	11.3	10.4 – 12.3	11.3
Mg I	15.0 – 15.4	15.2	14.7 – 15.0	14.8	14.6 – 15.2	14.8
Mg II	17.6 –17.9	17.7	17.6 – 18.1	17.9	17.2 – 18.0	17.6
Fe II Low[h]	16.7 - 17.0	16.8	16.9 – 17.3	17.2	16.6 – 17.3	16.9
Fe II High[i]	13.2 – 14.5	13.8	11.6 – 14.1	12.8	11.5 – 14.6	12.7

Table 3—Continued

Parameter	Constant Pressure		Density Jump = 0.6[a]		Density Jump = 1.4[a]	
	Range[b]	Characteristic Solution[c]	Range[b]	Characteristic Solution[c]	Range[b]	Characteristic Solution[c]
Mn II	15.2 – 15.5	15.3	15.2 – 15.7	15.5	14.9 – 15.6	15.2
C IV	17.2 – 17.4	17.3	16.1 – 17.1	16.4	16.1 – 17.3	17.0
N V	16.8 – 17.0	17.0	15.5 – 17.3	16.0	15.5 – 17.5	17.1
Kinematic and Other Parameters						
[O III] Equivalent Width (Å)[j]	150 – 270	190	150 – 200	190	120 – 200	150
Outflow Radius (pc)	62 – 150	110	13 – 230	54	13 – 230	100
Outflow Mass Flux ($M_\odot\,yr^{-1}$)	600 – 2830	1410	170 – 4400	700	55 – 4400	740
log Kinetic Luminosity [$erg\,s^{-1}$]	45.6 – 46.3	46.0	45.0 – 46.4	45.6	44.5 – 46.5	45.7
Kinetic / Bolometric Luminosity	0.47 – 2.2	1.1	0.13 – 3.5	0.5	0.04 – 3.5	0.6

[a]The density jump is defined as the logarithmic factor by which the density increases at the hydrogen ionization front (§7.2).

[b]The range of the parameter for solutions where $MFOM = 0$.

[c]The characteristic or typical value (see §6.3 for a description of how this parameter is calculated).

[d]Simulation range: $-1.5 < \log U < 0.5$ for constant pressure, $-2.0 < \log U < 1.0$ for density step simulations.

[e]Simulation range: $3.0 < \log n < 5.5$.

[f]The dust-to-gas ratio parameter is the fraction of the normal dust to gas ratio for the ISM. Simulation range: 0.05 to 0.3. See §6.3 for details.

[g]The abundance parameter is the logarithmic fraction of the normal ISM depletion. Simulation range: 0.3 to 0.8. See §6.3 for details.

[h]Column density of Fe^+ atoms populating energy levels up to 0.12 eV above the ground state. A strong feature in the near UV from transitions from these levels appears between 2585 and 2631Å. See Lucy et al. (2014) for details.

[i]Column density of Fe^+ atoms populating energy levels between 0.98 and 1.1 eV above the ground state. A strong feature in the near UV from these levels appears between 2692 and 2773Å. See Lucy et al. (2014) for details.

[j]Assumes global covering fraction of 0.2.

This figure has several interesting features. First, our constant stopping criterion of A_V plus dust-to-gas ratio specifies a hydrogen equivalent column density. Thus, the $\log U$ vs $\log n$ graph (Fig. 9, left side) shows values for a constant $\log N_H = 22.7\,\mathrm{cm}^{-2}$. Second, since $U = \phi/nc$, where ϕ is the photoionizing flux, contours of constant photoionizing flux run diagonally across the plot, along the contours. Constant photoionizing flux occurs at constant radius. Thus, our $MFOM = 0$ solutions all lie approximately the same distance from the central engine.

Fig. 10 shows contours of ionic column density as a function of the simulation parameters, also orthogonal to the characteristic solution. These graphs show how the various lines constrain the simulation parameters. Neutral sodium is strongly dependent on the ionizing flux. For a fixed column density, the lower the photoionizing flux, the more likely that a predominately neutral zone, necessary for neutral sodium to survive, will be present at the back of the slab. Neutral sodium depends inversely on the dust-to-gas ratio; the larger the gas fraction, the thicker the gas for the fixed value of A_V, and thus the more likely a neutral zone will be present at the back of the slab.

He I* shows interesting ionization parameter/density dependence. For low values of photoionizing flux (low values of $\log U$ and $\log n$), the He I* first increases as photoionizing flux increases. As discussed in Leighly et al. (2011) and elsewhere, the amount of He I* depends on the thickness of the He^+ region, which increases as ϕ increases. But for higher values of ϕ (high values of $\log U$ and $\log n$), He I* decreases, the opposite of what would be expected for dust-free gas (e.g., Leighly et al. 2011). This happens because, as ϕ increases, the He^+ region is shifted toward the back of the slab, where the accumulated extinction, proportional to depth in the slab, is higher. The increased extinction removes photons in the helium-ionizing continuum, and so there is less He^+ produced, and consequently less He I*. There is no dependence on depletion, since helium is not depleted onto grains,

and the dependence on dust-to-gas ratio mirrors the column density variation with this parameter, coupled with the extinction.

The low-ionization ion Ca^+ has similar dependence on ionization parameter and density as neutral sodium. It has, however, stronger dependence on depletion than any of the other ions. This is because calcium is the most strongly depleted onto dust of all elements.

Finally, hydrogen in $n = 2$ strongly depends on photoionizing flux. The lack of Balmer absorption lines is generally a good density indicator; we used this to obtain a density upper limit for FBQS J1151+3822 in Leighly et al. (2011) and Lucy et al. (2014). In this case, however, the combination of Na I and He I* provide stronger constraints on the photon flux and therefore density.

Thus, the lines play complementary roles in constraining parameter space. The neutral sodium, Balmer lines and Ca II push the solution toward lower photon fluxes, and therefore lower values of ionization parameter and density. In contrast, the He I* pushes the solution toward higher photon fluxes, and correspondingly higher values of ionization parameter and density. Ca II, since it is so much more sensitive to depletion compared with the other elements, constrains the depletion parameter. And a low dust-to-gas ratio is required in order to accumulate a large enough column density to produce a sufficient column of low-ionization lines without exceeding our stopping criterion $A_V = 2$.

6.4. Constraints on Outflow Properties

We compute the kinematic and other properties of the 35 $MFOM = 0$ solutions, using equations 9 and 11 in Dunn et al. (2010). The results are listed in the first pair of columns of Table 3. The radius of the outflow for the $MFOM = 0$ solutions lies between 62 and 147 parsecs, with a characteristic value of 110 parsecs. The outflow location is strongly

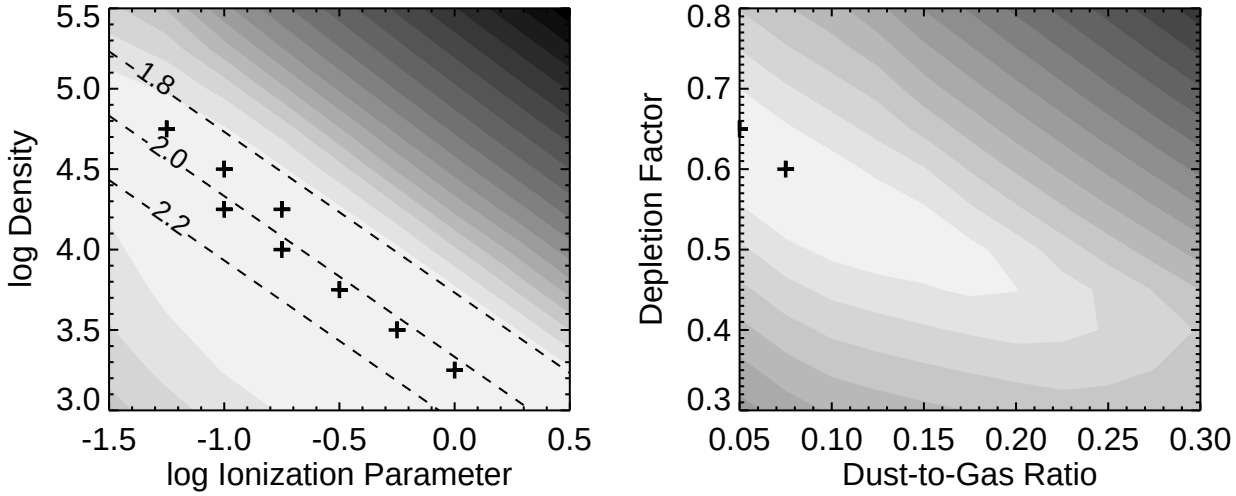

Fig. 9.— Contours of the modified figure of merit (MFOM) as defined in §6.3 as a function of simulation parameters, for a fixed $A_V = 2$, in orthogonal directions to the characteristic solution ($\log(U) = -1.5$, $\log(n) = 3.75$, dust-to-gas scale factor equal to 0.075, and depletion scale factor of 0.6). The plus signs show where $MFOM = 0$, i.e., where the solutions are consistent with the limits and bounds (§6.3). The dashed lines show contours of constant log distance of the absorber from the central engine, in units of parsecs. So, the solutions imply that the absorber lies $\sim 100\,\mathrm{pc}$ from the central engine, near the location of the circumnuclear starburst (e.g., Davies et al. 2004).

anticorrelated with $\log(n) - \log(U)$, i.e., the photon flux, underlying the strong dependence on this parameter, as discussed §6.3. The log hydrogen column density $[\,\mathrm{cm}^{-2}]$ is between 22.6 and 22.9, and is strongly anticorrelated with the dust-to-gas ratio. That is, a large column density is needed to reach the stopping criterion $A_V = 2$ if the dust-to-gas ratio is low; at the same time, high dust-to-gas ratios are ruled out by the necessity of having sufficient photoionizing photons to produce the observed He I*.

We used $4,500\,\mathrm{km\,s^{-1}}$ as a characteristic outflow velocity. It is not obvious what value of the global covering fraction we should use. On one hand, the reddening scheme discussed in §3 implicitly requires a large covering fraction approaching $\Omega = 1$. On the other hand,

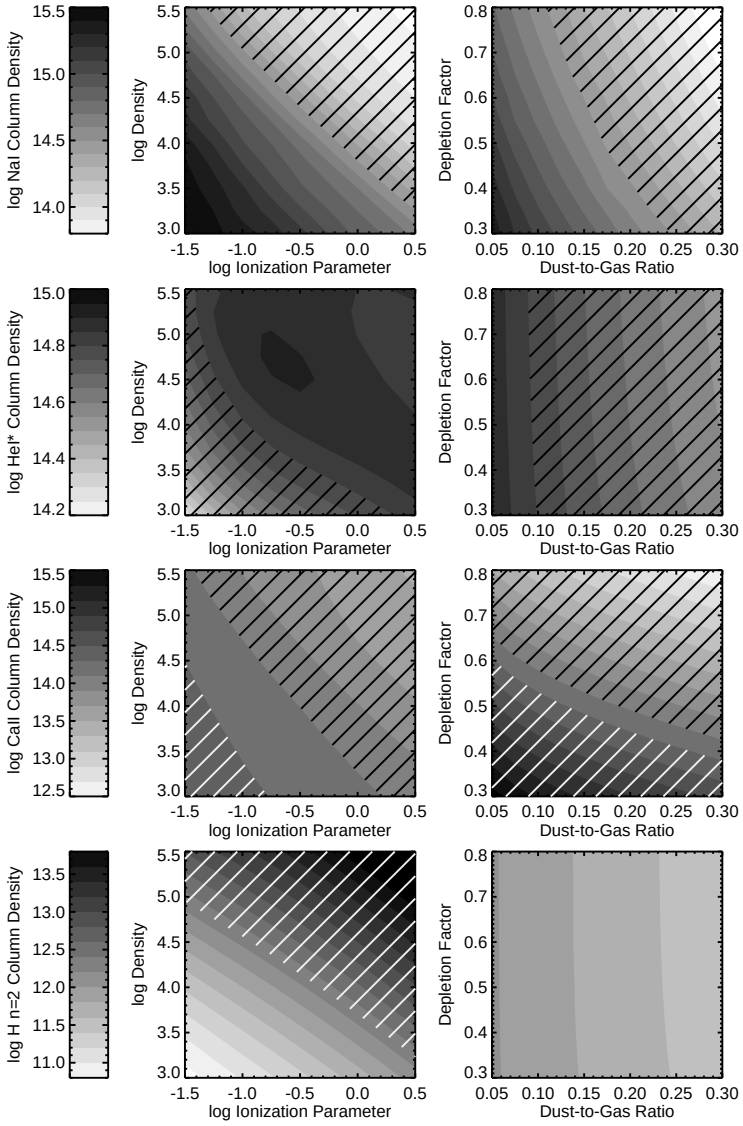

Fig. 10.— Contours of ionic column density as a function of the simulation parameters, for a fixed value of $A_V = 2$, in orthogonal directions from the characteristic solution ($\log(U) = -1.5$, $\log(n) = 3.75$, dust-to-gas scale factor equal to 0.075, and depletion scale factor of 0.6). From the top to the bottom, we should results for Na I, He I*, Ca II, and H I in $n = 2$. The hatched areas show regions not consistent with the limits or bounds, where black hatches indicate a lower limit, and white hatches indicate an upper limit. See §6.3 for discussion.

it is not clear that the interaction between the BAL wind and starburst gas, as outlined in §6.2 occurs along all lines of sight. So for comparison with other results, we assumed the rather standard value of the global covering fraction $\Omega = 0.2$, based roughly on the fraction of quasars observed to have broad absorption lines (e.g., Dunn et al. 2010).

We obtain very large values of mass fluxes between 600 and 2830 $\mathrm{M_\odot\,yr^{-1}}$ compared with other BAL quasars with detailed kinematic analysis (e.g., Table 10 Dunn et al. 2010). Likewise, we also obtain very large values for the kinetic luminosity, with $\log \dot{E}_k$ between 45.6 and 46.3. These large values of kinetic luminosity lead to very large values of the ratio of the kinetic luminosity to the bolometric luminosity, between 0.47 and 2.2. While such large values imply that the outflow system in Mrk 231 is capable of vigorous feedback, it is not clear whether acceleration mechanisms could produce such large values, especially values greater than 1.

These extremely large values of mass flux, kinetic luminosities, and ratio of kinetic to bolometric luminosities occur principally because of the very large column densities necessary to produce the Na I absorption. The radius is not exceptionally large compared with other quasars that have apparently low density outflows in which kiloparsec-scale outflows can be found (e.g., Table 10 in Dunn et al. 2010). The column density is, however, two to three orders of magnitude larger than typical column densities found for the kpc-scale outflow (e.g., 19.9–20.8, Table 10, Dunn et al. 2010). The kinetic luminosity and mass flux depend linearly on column density, so for those objects, the log kinetic luminosity ranges from 43.7 to 45.7. More recently, Arav et al. (2013) inferred a kinetic luminosity of $10^{45}\,\mathrm{erg\,s^{-1}}$ for the quasar HE 0238−1904. However, their column density estimates were still rather low (19.8–20.9), and the ratio of the kinetic luminosity to the bolometric luminosity was only 1% for that very luminous quasar.

6.5. [O III] Line Emission

The density of the illuminated side of the gas slab in our simulations is low, similar to densities present in the narrow-line region of AGN. These low densities yield $MFOM = 0$ because the solutions tend to lie along constant values of ionizing flux. High densities correspond to low values of ionization parameter, which do not produce sufficient He I*. At any rate, for the favored low values of density, the H II region of the outflow, at least, can be expected to emit lines characteristic of the NLR. For reference, the critical density for [O III]λ5007, one of the brightest NLR lines, is $6.8 \times 10^5\,\mathrm{cm}^{-3}$ (Osterbrock & Ferland 2006). Even in pressure balance, there is a considerable amount of gas in our simulations with densities smaller than that value. Thus, our outflows can be expected to produce line emission. We emphasize that this putative [O III] emission should be distinguished from NLR [O III] emission, which is often observed to be relatively weak in BALQSOs (e.g., Boroson 2002), and is not observed at all in Mrk 231.

We extracted the [O III] fluxes from the *Cloudy* simulations, and then computed the equivalent width with respect to the *Cloudy* transmitted continuum. This continuum is an approximation for our physical situation, as it is computed using slab reddening, where as, as we have shown in §3, the extinction in Mrk 231 is more appropriately circumstellar. However, since the result is not subtle, the transmitted continuum served our purpose. Assuming again a global covering fraction $\Omega = 0.2$, we found a range of equivalent widths between 146 and 270Å. This would be a very strong line that is clearly not seen in the spectrum.

There are several ways in which the predicted [O III] line could be hidden. First, the velocity of the absorption line is the radial component of the velocity along our line of sight. The global outflow, if present, would be expected to be directed in a range of directions, yielding a range of radial velocity components. That would smear the line, decreasing its

contrast with the continuum. Second, it is not clear that we would be able to see all of the line emission. That is, emission in the receding wind on the far side of the object may be attenuated by dust. So even if $\Omega = 0.2$, we may be able to see only a small fraction of that. Finally, it is possible that the global covering fraction is much less than $\Omega = 0.2$. Mrk 231 is not a typical BALQSO, and thus its geometry and physical conditions cannot be expected to conform with the expectations of the general population. Nevertheless, the possibility of forbidden line emission from low-density ($n \approx 10^4\,\mathrm{cm}^{-3}$) BAL outflows is interesting, and possibly constraining, and to our knowledge, previously unexplored.

6.6. Properties of the Characteristic Solution

The modified figure of merit identifies a region of parameter space in which the upper and lower limits and parameter bounds for the four diagnostic ions are met. As discussed above, we identified a characteristic solution among the set of solutions that satisfy $MFOM = 0$. That solution is characterized by $\log U = -0.5$, $\log n = 3.75$, dust-to-gas ratio parameter equal to 0.075, and depletion parameter equal to 0.6. At this point, the absorbing gas lies 110 pc from the nucleus, and the inner edge of the torus, characterized by $R_{\tau K} = 0.31\,\mathrm{pc}$, would subtend an angular diameter of about 19 arcminutes. As shown in Table 3, the log outflow kinetic luminosity would be 46.0, and the ratio of kinetic to bolometric luminosity would be 1.1.

Plots of interesting parameters for the characteristic solution are shown in Fig. 11. The left panel shows the temperature and density as a function of depth through the slab. As the photoionizing continuum traverses the slab, electrons are liberated, heating the gas. Eventually, the continuum runs out of photons able to ionize hydrogen, the number of photo-electrons decreases, and the gas becomes much cooler, especially beyond the hydrogen ionization front, located, for this simulation, at 6.9×10^{17} cm from the illuminated

side of the slab. In this constant pressure simulation, the drop in temperature must be compensated by an increase in density. Thus, the gas at the back of the slab has, in effect, a much lower ionization than it would in a constant density simulation.

The central panel of Fig. 11 shows the location of the optical and infrared absorbing ions in the illuminated slab. He I* is formed by recombination onto He^+, so it is coincident with that ion. The low-ionization lines Ca II and Na I instead originate in the partially-ionized zone where hydrogen is predominately neutral. Although the full slab has a thickness of 0.24 pc, the region where the lines discussed in this paper are formed has a thickness of only 0.027 pc. Note that other higher-ionization lines, e.g., N V, would be formed at shallower depths.

The right panel shows the cumulative ion fraction and [O III] emission as a function of the hydrogen column density, further illustrating the location difference in the line-forming regions among the ions. It also illustrates that, because of the density gradient, most of the gas is located in the region where the optical and infrared lines are formed. The He I* nearly saturates abruptly at rather small column densities; interestingly, some He I* (and likewise He^+) is present beyond the hydrogen ionization front, which is located in this simulation at a hydrogen column density of $8.8 \times 10^{21}\,\mathrm{cm}^{-2}$. We don't understand why this happens, since in many AGN photoionization scenarios, the continuum runs out of helium-ionizing photons (ionization potential equal to 24.6 eV) before it runs out of hydrogen ionizing photons (ionization potential equal to 13.6 eV).

6.7. Other Absorption Lines

In this paper, we discuss only the absorption lines observed in the optical and infrared. Other absorption lines, including those from Fe II, Mg II, and Mg I, have been

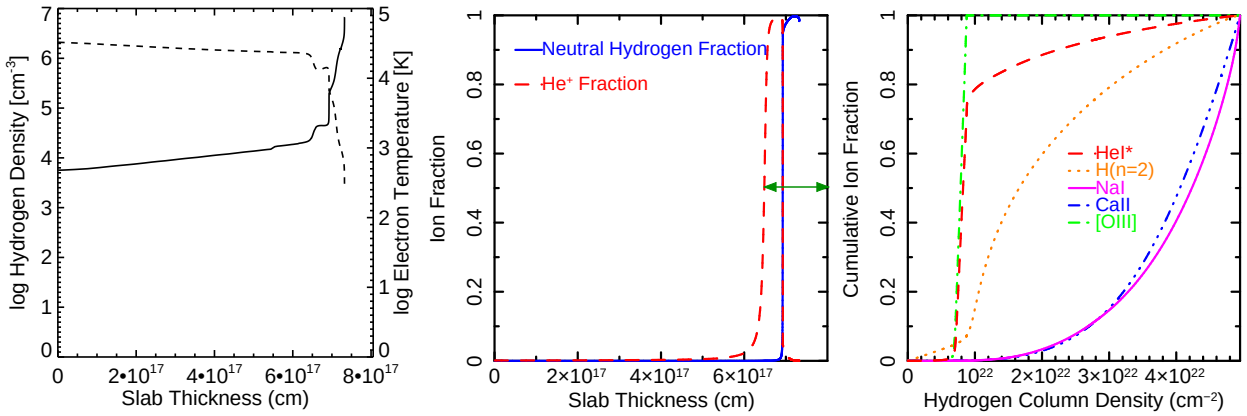

Fig. 11.— Physical properties of the characteristic solution, specified by $\log U = -0.5$, $\log n = 3.75$, dust-to-gas ratio parameter equal to 0.075, and depletion parameter equal to 0.6. *Left:* The variation of the hydrogen density (solid line) and the electron temperature (dashed line), as a function of depth in the illuminated slab. In this constant-pressure simulation, as the temperature drops, the density increases. *Middle:* The location of the absorbing ions. Metastable helium, which produces He I*$\lambda, \lambda 3889, 10830$ is produced principally by recombination onto He^{+}. The Na ID, Ca II, and undetected Balmer lines are produced in the partially-ionized zone, coincident with the region beyond the Stromgren sphere and dominated by neutral hydrogen. Thus, while the full slab has a thickness of 0.24 pc, the region of the slab where observed lines are formed (marked in green) has a thickness of only 0.027 pc. *Right:* The cumulative, normalized ion fraction as a function of hydrogen column further illustrates that the He I* absorption originates in different gas than the low ionization absorption Na ID and Ca II. [O III] (§6.5) cumulative emissivity is also shown.

reported by Smith et al. (1995), while a broad C IV line was reported by Gallagher et al. (2002). In principle, better constraints on our photoionization model could be obtained by combining the near-UV line measurements with the optical and infrared line measurements. However, both UV spectra have very poor signal-to-noise ratios, making constraint of the continuum and measurement of the absorption lines quite difficult. The second, possibly more important issue is that the partial covering may be wavelength dependent, making absorption lines appear shallower than they really are. There is no reliable way to estimate

the covering fraction with the data at hand if it is wavelength dependent. Newly approved *HST* COS and STIS observations may provide much better constraints than the archival data.

Nevertheless, we discuss one particular line to illustrate the potential problems. Smith et al. (1995) show a clear detection of Mg Iλ2852 in their FOS spectrum. But the line does not appear to be very broad or deep, at least compared with the Na ID line. Smith et al. (1995) does not provide an estimated limit on Mg I column density, so we estimate it from the reported equivalent width and the digitized spectrum, finding a lower limit on the log column density of ~ 11.3, much smaller than the measured Na ID column. However, our *Cloudy* models (Table 3) predict a range of Mg I log column densities between 15.0 and 15.4, similar to the Na I column densities. One possible explanation for this discrepancy is that the covering fraction of the nuclear starburst is higher in the NUV than it is for the continuum source. (This is conceivable, for example, if the starburst is the origin of the circumstellar dust). That could make the Mg I absorption line appear much shallower than the optical and IR lines, leading to a low estimate of the column density. Mrk 231 is close enough that the nuclear starburst can be resolved, and so it may be possible to probe differential reddening/covering for the nuclear emission versus the starburst emission with the upcoming 1-orbit *HST* STIS observation.

Likewise, the *Cloudy* models predict other common UV BAL lines to have high column densities. For example, C IV is predicted to have a log column density of between 17.2 and 17.4. This line would be saturated. The only line predicted to be somewhat weak is "Fe II High", as we refer to the transitions between 2692 and 2773 Å that arise from levels between 0.98 and 1.1 eV above the ground state (Lucy et al. 2014). Those excited-state Fe II atoms are predicted to have a log column density between 13.2 and 14.5, while the transitions near the ground state ("Fe II Low") are predicted to have log column density of

16.7–17.0. This happens because many of the excited-state Fe II transitions have relatively high critical densities (e.g., higher than $10^5\,\mathrm{cm}^{-3}$, Korista et al. 2008). Our gas has too low density to promote many of the iron ions to the excited states. Depending on the width of the absorption lines, it is then possible that Fe II High would not be saturated.

7. Beyond the Initial Model

In §6.3, we showed that we could obtain a family of solutions that produced the ionic column densities that we measured and are consistent with upper and lower limits. However, we needed to make a series of assumptions to construct this model. In this section, we investigate the consequences of these assumptions, one by one, to determine how they influence the location, energetics, and other properties of the absorber.

7.1. Dust in *Cloudy*

The current version of *Cloudy* is quite sophisticated and flexible in its handling of dust. Several dust models are built in, and a user may even input his or her own dust model. As noted above, we used the built-in ISM dust for our simulations, since Milky Way dust was favored in our reddening analysis (§3). It may be that the dust in Mrk 231 has much different absorption and scattering properties than Milky Way dust, given that it is subject both to the quasar continuum and the nuclear starburst. Qualitatively, for example, a different type of dust may produce a smaller or larger extinction in the helium continuum. That would increase or decrease our inferred dust-to-gas ratio, to meet the requirement that sufficient photons remain in the He^+ continuum to produce the observed He I* column density.

Despite this flexibility, the *Cloudy* user cannot specify variable dust properties (i.e.,

variable dust-to-gas ratio) as a function of depth of a slab. As discussed in §6.2, based on the kinematic differences between the He I* lines and the low-ionization lines Ca II and Na I, we suggested that the H II region of the outflow is a traditional BAL wind, and is therefore relatively free of dust. But dust must be present in the H I region of the outflow, since depletion is necessary to explain the Ca II column density. If the H II region were dust free, more He I* would be produced since, as discussed in §6.3, when dust is present, He I* is suppressed for high photon fluxes as the He I continuum is depressed by extinction.

Is dust necessary in the *Cloudy* simulation? That is, perhaps all of the absorption occurs interior to the circumstellar scattering region, in which case the absorber may be free of dust. To test this possibility, we ran several dust-free models, starting at the parameter values of the characteristic solution, but using a range of hydrogen column densities as the stopping criteria. We find that a log hydrogen column density of 23.7 is necessary to produce the lower limit on the Na I. This an order of magnitude larger than the column density inferred from the characteristic solution. This model also produced insufficient calcium, although that could be addressed by adjusting the depletion. Regardless, an order-of-magnitude larger column density would predict an order of magnitude larger kinetic luminosity, making an inferred kinetic luminosity many times larger than the bolometric luminosity.

Another issue is that while we used circumstellar dust to explain the reddening, the *Cloudy* models use slab-type dust. It is clear that the circumstellar reddening cannot be present throughout the absorbing gas because the extremely strong blue extinction would remove all the He^+ continuum photons, and insufficient He I* would result. However, we may imagine again that the H II region, where the He I* absorption is produced, lies inward to the scattering region, and the partially-ionized zone lies in gas in which the circumstellar reddening is appropriate. Due to strong blue opacity, the partially-ionized zone may have a

very low skin-depth, transitioning very quickly to gas in which neutral sodium and Ca^+ can exist. Then, it is possible that the required absorption lines could be produced with smaller column density, and perhaps no density increase would be required. We cannot simulate this situation with the tools at hand, however.

7.2. The Constant Pressure Assumption

In §6.3, we assumed constant pressure in our *Cloudy* model in order to provide a density gradient. However, constant pressure is not likely to be physically realistic. First, the outflow velocity is much greater than the speed of sound (approximately $10\,\mathrm{km\,s^{-1}}$ in the H II region) so it is not clear how pressure equilibrium would be attained in the dynamical environment. Second, as discussed in §4, there is evidence from the line profiles that the inner gas is moving radially outward with a larger velocity than the outer gas, and we suggested (§6.2) a scenario in which the inner gas from an quasar BAL wind impacts and scoops up processed gas from the starburst. In this case, a shock may be present; alternatively, the processed gas may have higher density than the BAL wind.

It turns out, however, that we do not need to assume constant pressure to obtain the measured ionic column densities; all we need is a density increase between the He I* absorbing gas, and the Na I absorbing gas. To test how much of a density increase is necessary, we ran a series of *Cloudy* models using density laws, i.e., we specified density as a function of depth from the illuminated side of the gas slab. To build the parameterized density laws, we started with the characteristic solution, assuming constant pressure, and extracted the density as a function of depth. Since He I* is produced in the H II region and the low ionization lines are produced in the partially-ionized zone, we placed the density increase at the hydrogen ionization front. We retained the density profile in the H II region, since we know that it provides the required amount of He I*. We modified the density in the

partially-ionized zone, assuming a constant value throughout, for a range of multiplicative enhancement factors relative to the density in the region where He^+ is found (for example, for the characteristic solution, $\log(n) = 4.66$ at this point). This density profile is ad hoc, although one might imagine that an approximate step function density profile could be obtained in a shock.

For no or little density enhancement, the sodium column is low, too low to produce a detectable Na I absorption line. We find that an enhancement by a multiplicative enhancement factor of 14.5 (i.e., increase to a log hydrogen density of 5.8) will yield required Na I column. So, although the constant pressure solution illustrated in Fig. 11 indicates a density jump of ~ 1000 from the illuminated side to the back end, in fact, we only really need a factor of 14.5 to explain the Na I column density.

7.3. Elevated Abundances

If the swept-up gas originates in the nuclear starburst, the abundances may be modified by the stellar processing. AGB stars can eject gas with large enhancements in abundances (e.g., Kraft 1994), depending on the length of time in certain evolutionary states. For example, in the most favorable case, sodium can be enhanced by a factor of 100.

We computed an altered abundance pattern by assuming that the starburst rapidly used up all the gas in the central regions of the Mrk 231, and that the gas contained in the AGN outflow was entirely the product of enriched mass loss from those stars that became Type II supernovae (SN) or AGB stars before some designated time. We took AGB yields from Karakas (2010) and yields for more massive stars from Chieffi & Limongi (2004), and we linearly interpolated the yields for the various elements as a function of stellar mass between the two studies. In all cases we used the yields from solar-abundance models. The

computation assumed a Salpeter (1955) mass function with $x = -2.35$, and we took the age since the starburst as 100 Myr (cf. Fig 6); this sets the lower mass limit in the computations to $4M_{\odot}$, which is the mass of a star with this lifetime in the Karakas models. We computed both the combined AGB + SN case and (for comparison) AGB-only enrichment. The former computation used an upper mass bound of $20M_{\odot}$, while the upper bound for the latter case was set at $7M_{\odot}$. The luminosity-function weighted yields were most sensitive to the upper bound for the combined case, but did not depend strongly on the lower mass limit. The resulting abundance enhancements relative to hydrogen are listed in Table 4.

We tested the effects of these enhanced abundances on the characteristic solution. We assumed that the gas is purely reprocessed gas from the starburst, i.e., with no un-reprocessed gas mixed in, and therefore, these numbers represent the maximum enhancement we could expect. For the low-mass stellar evolution scenario, the He I* column was increased by 0.15 dex and the Na I was increased by 0.22 dex. When the higher mass stars are included, we found He I* enhancement by 0.3 dex and Na I enhancement by 1.34 dex (i.e., a factor of 22 times larger). In both cases, Ca II and H I in n=2 remained in observed bounds.

The effect of these enhancements is to expand the allowed region of parameter space. As discussed in §6.6, the $MFOM = 0$ solutions are found in a narrow band of photoionizing flux (and therefore radius) because of the opposing constraints provided by the He I* and Na I columns on this parameter. The stellar reprocessed gas has enhanced abundances for both helium and sodium, and thus the column densities for both parameters are increased. Since the criterion for both parameters is a lower limit, the effect is that a broader range of photoionizing fluxes produce column densities in the acceptable range.

The second effect is to permit $MFOM$ solutions with a larger value of dust-to-gas ratio. The dust-to-gas ratio in the characteristic solution was constrained to be low so that

Table 4. Fractional Abundance Enhancements in 100 Myr Starburst

Isotope	AGB[a]	AGB/1H[b]	AGB+SN[c]	AGB+SN/1H[d]
1H	0.918	1.000	0.850	1.000
4He	1.191	1.298	1.255	1.477
12C	0.851	0.927	1.873	2.203
14N	5.502	5.995	4.955	5.830
16O	0.869	0.947	1.896	2.231
20Ne	1.000	1.089	5.716	6.725
22Ne	2.542	2.770	7.148	8.410
23Na	1.709	1.862	11.346	13.350
24Mg	0.980	1.068	2.635	3.100
27Al	1.061	1.156	2.961	3.484
28Si	1.004	1.094	6.067	7.138
32S	0.996	1.086	4.436	5.219
34S	1.003	1.092	1.394	1.640
56Fe	0.995	1.085	2.186	2.573

[a]Ratio of isotope to solar abundance assuming a mass function slope of -2.35 for a 100 Myr starburst including AGB stars down to 4 solar masses.

[b]Ratio of isotope to solar abundance normalized to the hydrogen ratio assuming a mass function slope of -2.35 for a 100 Myr starburst including AGB stars down to 4 solar masses.

[c]Ratio of isotope to solar abundance assuming a mass function slope of -2.35 for a 100 Myr starburst including AGB stars down to 4 solar masses and Type II supernovae.

[d]Ratio of isotope to solar abundance normalized to the hydrogen ratio assuming a mass function slope of -2.35 for a 100 Myr starburst including AGB stars down to 4 solar masses and Type II supernovae.

there were sufficient photons in the helium continuum to produce the observed He I*. A low dust-to-gas ratio also contributes in allowing sufficient column density to reach the neutral gas in which the Na I column is produced. A larger dust-to-gas ratio would lead to a lower hydrogen column density, and a lower inferred kinetic luminosity.

7.4. Continuum Shape Assumption

The simulations presented here employ the *Cloudy* "Kirk" continuum, suggested as a representative AGN continuum by Korista et al. (1997). This continuum is fairly hard, with an α_{ox} measured from the continuum of -1.45. Based on our inferred intrinsic 2500Å monochromatic luminosity of $1.2 \times 10^{30}\,\mathrm{ergs\,s^{-1}\,Hz^{-1}}$, and the relationship between UV luminosity and α_{ox} presented by Just et al. (2007), an $\alpha_{ox} = -1.51$ would be predicted for Mrk 231. Evidence has been increasing that at least some BALQSOs have intrinsically X-ray weak spectral energy distributions (e.g., Sabra & Hamann 2001; Clavel et al. 2006; Grupe et al. 2008; Luo et al. 2013). Mrk 231 was recently observed in the X-ray using *Suzaku* by Piconcelli et al. (2013), who reported an increase in X-ray flux and appearance of the primary continuum at $< 10\,\mathrm{keV}$. They recorded an intrinsic 2–10 keV luminosity of $3.3 \times 10^{43}\,\mathrm{erg\,s^{-1}}$. Assuming that the intrinsic spectrum can be described by a $\Gamma = 1.9$ power law, an $\alpha_{ox} \approx -1.7$ is inferred. Recently, a value of $\alpha_{ox} \sim -1.7$ was measured using *NuSTAR* data (Teng et al. 2014). Therefore Mrk 231 is now known to be intrinsically X-ray weak.

As discussed in Leighly et al. (2011, Appendix A), a higher column density is generally required to produce a large He I* column when the continuum is soft, simply because soft continua lack photons in the He^+ continuum ($> 24\,\mathrm{eV}$) that are needed to ionize helium. In other words, a more intense continuum and thicker column would be required to produce the same He I* column for a softer continuum. For example, for the semi-empirical spectral

energy distributions introduced in Casebeer et al. (2006) and used in Leighly et al. (2007) and Leighly et al. (2011), an $\alpha_{ox} = -1.7$ continuum requires 0.2 dex higher column density, and a 0.4 dex higher photon flux to produce the same He I* column density as a $\alpha_{ox} = -1.4$ continuum. From a photoionization model point of view, a higher column density might be difficult to muster, given that in the dusty model, a higher column will incur more reddening, or, alternatively, since our stopping criterion in the simulations is the reddening, a lower dust-to-gas ratio.

However, these results depend on the precise shape of the continuum. The Casebeer et al. (2006) SEDs link the UV cutoff with the UV luminosity through α_{ox} according to $T^{1/4}$ (see Casebeer et al. 2006, for details). If, for example, the UV emission remained unchanged, but the coronal X-rays were weak or missing (a possibility that has been suggested recently for two BALQSOs based on recent *NuSTAR* results; Luo et al. 2013) it may still be possible to produce strong He I*. We tested this possibility by performing *Cloudy* modeling using a modified version of the"Kirk" AGN *Cloudy* to be weaker in the X-rays, created by simply cutting the spectrum at a particular energy, and then decreasing the flux shortward of that point by a multiplicative factor. To maximize the effect, we first varied the energy of the cut point, and determined the value required to produce most (within 97%) of the He I* obtained using the unmodified spectrum. That energy was $\sim 45\,\mathrm{eV}$. We then tried two continua, created by decreasing the normalization for $E > 45\,\mathrm{eV}$ by factors of 10 and 100. These continua are ad hoc, but considering that the shape of the extreme UV continuum is not known, they served to test the effect. We used the parameters of the characteristic solution as the starting point, but retained the normalization of the spectrum. The ionization parameter was then decreased from -0.5 to -0.61 and -0.62 for the continua attenuated by factors of 10 and 100, respectively.

We found that the He I* column density of the modified spectra actually increased

over that of the unmodified spectra. Specifically, the unmodified spectrum yielded a He I* log column density of 14.83, but the spectra cut by factors of 10 and 100 yielded He I* columns of 15.14 and 15.23, respectively. Examination of the simulation results show that these X-ray weak continua shift the overall ionization of the gas to intermediate- and low-ionization lines. A similar effect was seen in simulations of emission lines of the X-ray weak quasar PHL 1811 (Leighly et al. 2007). The sodium column density, on the other hand, decreased to 14.73 and 14.78, corresponding to −0.089 and −0.071 dex, respectively. These small changes imply that the factor most important in determining the Na I column density is how much of the sodium is ionized to Na^+, which is controlled by the strength of the spectrum shortward of 2412Å, and is unchanged in these simulations.

The increase in the simulated He I* column means that the acceptable parameter space would be expanded, specifically toward lower photon fluxes and therefore larger radii. To test the consequences of that shift, we ran a sequence of models while decreasing the overall continuum normalization. We found that the He I* was reduced to the non-modified-continuum level of the characteristic solution when the continuum decrease multiplicative factors were 5.4 and 7.3 for the 10 times X-ray weak and 100 times X-ray weak continua respectively. These models produce large column densities of sodium (larger by factors of 2.8 and 3.7 over the characteristic solution, respectively), and the other lines were consistent with the required limits and ranges. Also, like the abundance enhancement simulations, a larger value of dust-to-gas ratio would be allowed, corresponding to a reduced column density and kinetic luminosity.

8. Optimizing Parameters

Our initial model, described in §6, included a number of assumptions, and also resulted in a very large column density outflow, and correspondingly large and possibly unphysical

values of kinetic luminosity. In §7, we investigated these assumptions individually, specifically to see if modifying them would produce an outflow with lower column density. We found that a lower hydrogen column density could probably be attained if the gas abundances were modified by reprocessing by the starburst, or if the incident continuum were softer. In addition, we showed that constant pressure was not needed to obtain a satisfactory solution; rather, a modest step increase in density, such as might be produced in a shock, could also produce required ionic column densities.

In this section, we close the loop by running a full grid of models with a softer continuum and enhanced abundances, and using two density step-function enhancement factors. We then extracted a characteristic solution and range for these optimized parameter choices for each of the density step functions. Specifically, we used the soft continuum with the flux density decreased by a factor of 10 at energies > 45eV, and abundances modified by the medium-mass stars only. We test two density enhancement factors: 0.6 and 1.4. Thus, the density in the partially ionized zone increased by a factor of $10^{0.6} \approx 4$ and $10^{1.4} \approx 25$ with respect to the density in the He^+ zone at the hydrogen ionization front. The results are given in Table 3 and Figure 12.

In some respects, the solutions are very similar to our original solution. Specifically, the characteristic solution, i.e., the solution lying the minimum distance from all other $MFOM = 0$ solutions, is very nearly the same in all three cases. The larger difference lies in the ranges of parameters. In many cases, the range of parameters is larger for the density-jump simulations compared with the constant pressure simulation. This illustrates the fact that the softer continuum and enhanced abundances widens parameter space. Most significantly, the range of parameters, especially in the case of the larger density jump, encompass outflow kinetic energies that are arguably more reasonable (i.e., less than the bolometric luminosity) than those obtained in §6.4. At the same time, the characteristic

solutions are still all located $\sim 100\,\mathrm{pc}$ from the central engine.

The two density-jump solutions are distinctly different, however; this is best illustrated by Fig. 12. For a density jump by a factor of 4, the solutions are highly constrained in a narrow region of parameter space. These solutions require a small dust-to-gas ratio and correspondingly large column density, because the small density jump only modestly lowers the ionization parameter in the partially-ionized zone, and a large column density is therefore required to obtain the observed Na I column. In contrast, for a density jump by a factor of 25, parameter space is very large, the dust to gas ratio can be as large as 0.3 (the upper limit in the simulation grid), so the column density can be low. This is because the large density enhancement produces a low ionization parameter in the partially-ionized zone, and sufficient Na I can be produced at low column density.

All of the simulations presented in this paper lead us to conclude that a density gradient or jump is necessary to produce the observed He I* and the Na I ionic column densities. A larger question is, how much of a density jump could be produced in nature? If our surmise is correct, and the absorption lines are formed in the interaction region between the normal quasar outflow and the starburst, then in principle, the equations of motion could be written down and solved. In that case, the density jump incurred in the shock could be obtained.

We note that in the case of a supernova interacting with the circumstellar medium, the outflow velocities are similar and a high density gradient can be achieved. At minimum, we expect that the density contrast will be given by the Rankine-Hugoniot conditions and that for a gas with a ratio of heat capacities $\gamma = 5/3$, the density contrast would be $\frac{\gamma+1}{\gamma-1} = 4$. However, taking the analogy with supernovae further, higher density contrasts are possible. Chevalier & Fransson (1985) studied the density contrast obtained as a function of the density profile in the outflow. They assumed that the outflow density profile followed a

powerlaw $\rho \propto r^{-n}$ and that the circumstellar medium had a density profile of a constant velocity wind, $\rho \propto r^{-2}$. In this case they found that for $n = 20$, density contrasts can exceed 150. In fact, for very steep ejecta profiles $n = 50$, density contrasts can exceed 1000 (Chevalier & Fransson 1994). The steep density outflow profiles in supernovae are the natural result of the supernova shock running down the original steep profile that was established by hydrostatic equilibrium in the progenitor star, whereas in the case of an AGN the outflow will likely be accelerated. The material that the outflow runs into, however, should have a density profile not too far away from the r^{-2} of a constant velocity wind. Thus, it may not be too far afield to suggest that large density contrasts could occur.

9. Summary and Future Directions

We present the first J-band infrared, and new blue optical spectra of Mrk 231. Combining these with spectra taken from the literature, we discovered a physical solution for the unusual reddening in this object. *Cloudy* modeling revealed unusual physical conditions required to produce both He I* and Na I absorption lines in the same gas, and inspired a physical interpretation involving an interaction of a quasar BAL wind with gas ejected from a nuclear starburst. The specific results are as follows:

- We fit the broad band spectrum from ~ 2300 Å to $2.3\,\mu$m with a continuum model, a low-temperature black body, and a circumstellar reddening and extinction curve originally proposed to explain the low values of observed R_V in SNe Ia (Goobar 2008). Circumstellar reddening is distinguished by large optical depths, approaching 1, producing increased extinction in the blue & UV (due to longer scattering path lengths), along with light scattered back into the line of sight as a secondary effect. We obtained an excellent fit using extinction-shape parameters similar to those for Milky Way dust (§3). We suggested that the dust is produced in the nuclear starburst

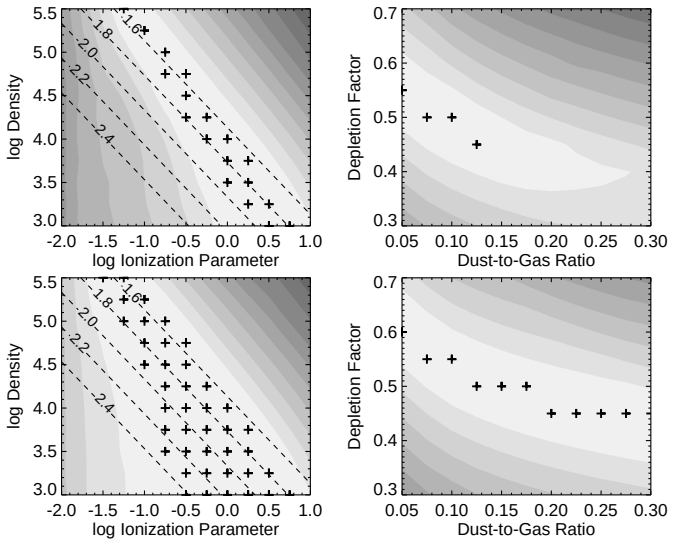

Fig. 12.— Contours of the modified figure of merit (MFOM) as a function of simulation parameters, for a fixed $A_V = 2$, in orthogonal directions to the characteristic solution (Table 3). These contours show the case described in §8, wherein the abundances were enhanced, the SED softened, and a density step was implemented, rather than constant pressure assumed. Note that to facilitate comparison with Fig. 9, the ionization parameter refers to the original continuum; the actual ionization parameters for the soft continuum are 0.11 dex lower. The plus signs show where $MFOM = 0$, i.e., where the solutions are consistent with the limits and bounds (§6.3). The dashed lines show contours of constant log distance of the absorber from the central engine, in units of parsecs. *Top:* The contours for a log density enhancement of 0.6. This panel shows that a solution can be found for a very modest density jump (factor of 4), but the parameters are very highly constrained. *Bottom:* The contours for a log density enhancement of 1.4. This panel shows that for a large density enhancement (factor of 25), parameter space opens up considerably.

lying $\sim 100\,\mathrm{pc}$ from the nucleus (e.g., Davies et al. 2004).

- The infrared spectrum revealed a deep He I* absorption line that is very similar in profile to the well-known Na I absorption line. Two newer infrared spectra revealed evidence for the appearance of a new absorption line component near $11,000\,\mathrm{km\,s^{-1}}$.

We modeled the optical and infrared spectra to extract the line profiles (§4.1, §4.2). After accounting for the $\sim 100\,\mathrm{Myr}$ nuclear starburst contribution, we inferred that the absorber essentially completely covers the quasar continuum emission region. The absorption line profiles indicated that the lines produced in the H II region, including He I*λ10830 and He Iλ3889, have a higher velocity than the low-ionization lines produced in the partially-ionized and neutral gas, including Ca II and Na I (§4.3).

- *Cloudy* modeling showed that in order to produce both the He I* and the Na I absorption lines, a density increase is required between the H II region, which produces the He I* lines, and the partially-ionized/neutral region, the origin of the Ca II and Na I lines. We first modeled this effect as a constant pressure gas (§6). The models are able to produce the measured column densities and limits if the gas lies $\sim 100\,\mathrm{pc}$ from the central engine, i.e., in the vicinity of the nuclear starburst (e. g., Davies et al. 2004). These facts, along with the velocity differences of the lines, and the inferred full covering, led us to a physical scenario in which the He I* absorption arises in a quasar BAL outflow that impacts and compresses dusty gas originating in the starburst, and this swept up gas is the origin of the Na I and Ca II lines (§6.2). In addition, we noted that just such an interaction between a quasar outflow and surrounding star-forming gas may be an example of quasar feedback, thought to be necessary to shut down star formation during the co-evolution of black holes and quasars.

- In §7 we examined the effects of modifying the assumptions made in our initial *Cloudy* model. In addition, the outflow masses and kinetic luminosities inferred were very large if the global covering fraction is $\Omega = 0.2$. Constant pressure gas may not be a reasonable assumption for a $\sim -4,500\,\mathrm{km\,s^{-1}}$ outflow, and therefore we instead experimented with a density increase between the H II region and the partially-ionized zone that might be physically realized in a shock, and found that a

density increase works as well as constant pressure. We discovered that the area of parameter space producing models consistent with the measurements is broadened when we consider abundances enhanced by stellar processing in the starburst, and when the spectral energy distribution is soft. We also suggested that the H II BAL outflow is free of dust, while the partially-ionized zone may have circumstellar dust. This situation, which could further reduce the inferred column density and therefore kinetic luminosity, cannot presently be modeled using *Cloudy* (which cannot model variable dust properties as a function of depth).

- Finally, in §8, we presented full grids using the optimal parameters obtained in §7. For a soft spectral energy distribution and enhanced abundances, a density enhancement by a factor of only four can still produce the lines we observe, although over a limited region of parameter space. A density enhancement by a factor of 25 opened up parameter space considerably. A shock would be expected to produce a density contrast of 4 for gas with $\gamma = 5/3$, and much larger density contrasts are inferred in supernovae, depending on the density profiles of the outflow and circumnuclear gas.

- Most of the simulations producing the observed ionic column densities favor low densities, i.e., $\log n \approx 4$. This density is characteristic of the narrow-line region in AGN. We find that, assuming a global covering fraction of $\Omega = 0.2$, the inferred equivalent width of the [O III] emission line should be 100–200Å. Such a huge line is not seen in Mrk 231. We note that the line may not necessarily be predicted to be sharp, but rather could be smeared by a range of line-of-sight velocities, or obscured by dust.

While we consider the question of the cause of the anomalous reddening essentially solved in this paper, a number of questions regarding the absorption lines remain. Some may be addressed by the upcoming *HST* observations of Mrk 231. For example, additional

UV and near-UV absorption line measurements may be able to further refine the *Cloudy* modeling; this may be complicated by differential continuum and starburst covering fractions and extinctions. Dynamical modeling may be able to determine whether shocks could produce density jumps as large as the simulations require. Further development of *Cloudy* may ultimately allow specification of dust properties as a function of depth into the gas slab. In addition, our models are 1-D, and so cannot explicitly take into account the effect of the circumstellar reddening on the photoionization results. At any rate, the unusual set of circumstances required to produce the observed optical and infrared absorption lines may explain why Na I lines are so rare, or at least why the line in Mrk 231 is so exceptional; without the interaction of the BAL wind and starburst gas along our line of sight, Mrk 231 might instead look like an ordinary FeLoBAL quasar.

KML acknowledges very useful conversations with Dick Henry, Kieran Mullen, and Angela Speck, and useful comments from the OU Astro Journal Club. KML thanks Lucimara Martins for providing her starburst infrared spectral templates. KML gratefully acknowledges John Wisniewski's donation of APO time to the OU astronomy group, and thanks him for taking the April 7 2014 observations. KML and DMT thank OU Nielsen Hall system administrator Andy Feldt for copious help and advice in using the NHN Condor queue. KML and ABL acknowledge support through NSF AST-0707703. The authors acknowledge Sara Barber's participation in the KPNO and IRTF observing runs. TIFKAM was funded by The Ohio State University, the MDM consortium, MIT, and NSF grant AST-9605012. The HAWAII-IR array upgrade for TIFKAM was funded by NSF Grant AST-0079523 to Dartmouth College.

Facilities: Mayall (R-C CCD Spectrograph), IRTF (SpeX), Hiltner, ARC: 3.5m (TripleSpec)

REFERENCES

Adams, T. F., & Weedman, D. W. 1972, ApJ, 173, L109

Arav, N., Borguet, B., Chamberlain, C., Edmonds, D., & Danforth, C. 2013, MNRAS, 436, 3286

Boksenberg, A., Carswell, R. F., Allen, D. A., et al. 1977, MNRAS, 178, 451

Boroson, T. A. 2002, ApJ, 565, 78

Boroson, T. A., & Meyers, K. A. 1992, ApJ, 397, 442

Boroson, T. A., Meyers, K. A., Morris, S. L., & Persson, S. E. 1991, ApJ, 370, L19

Bruzual, G., & Charlot, S. 2003, MNRAS, 344, 1000

Cardelli, J. A., Clayton, G. C., & Mathis, J. S. 1988, ApJ, 329, L33

Casebeer, D. A., Leighly, K. M., & Baron, E. 2006, ApJ, 637, 157

Chevalier, R. A., & Fransson, C. 1985, in Lecture Notes in Physics, Berlin Springer Verlag, Vol. 224, Supernovae as Distance Indicators, ed. N. Bartel, 123–129

Chevalier, R. A., & Fransson, C. 1994, ApJ, 420, 268

Chieffi, A., & Limongi, M. 2004, ApJ, 608, 405

Clavel, J., Schartel, N., & Tomas, L. 2006, A&A, 446, 439

Cushing, M. C., Vacca, W. D., & Rayner, J. T. 2004, PASP, 116, 362

Dai, X., Shankar, F., & Sivakoff, G. R. 2008, ApJ, 672, 108

—. 2012, ApJ, 757, 180

Davies, R. I., Tacconi, L. J., & Genzel, R. 2004, ApJ, 613, 781

Deo, R. P., Richards, G. T., Nikutta, R., et al. 2011, ApJ, 729, 108

Draine, B. T., & Li, A. 2007, ApJ, 657, 810

Dunn, J. P., Bautista, M., Arav, N., et al. 2010, ApJ, 709, 611

Farrah, D., Afonso, J., Efstathiou, A., et al. 2003, MNRAS, 343, 585

Farrah, D., Urrutia, T., Lacy, M., et al. 2012, ApJ, 745, 178

Faucher-Giguère, C.-A., Quataert, E., & Murray, N. 2012, MNRAS, 420, 1347

Ferland, G. J., Korista, K. T., Verner, D. A., et al. 1998, PASP, 110, 761

Ferland, G. J., Porter, R. L., van Hoof, P. A. M., et al. 2013, Rev. Mexicana Astron. Astrofis., 49, 137

Forster, K., Rich, R. M., & McCarthy, J. K. 1995, ApJ, 450, 74

Gallagher, S. C., Brandt, W. N., Chartas, G., Garmire, G. P., & Sambruna, R. M. 2002, ApJ, 569, 655

Gallagher, S. C., Schmidt, G. D., Smith, P. S., et al. 2005, ApJ, 633, 71

Gibson, R. R., Jiang, L., Brandt, W. N., et al. 2009, ApJ, 692, 758

Goobar, A. 2008, ApJ, 686, L103

Goodrich, R. W., & Miller, J. S. 1994, ApJ, 434, 82

Grupe, D., Leighly, K. M., & Komossa, S. 2008, AJ, 136, 2343

Hall, P. B., Anderson, S. F., Strauss, M. A., et al. 2002, ApJS, 141, 267

Hamilton, D., & Keel, W. C. 1987, ApJ, 321, 211

Hewett, P. C., & Foltz, C. B. 2003, AJ, 125, 1784

Ho, L. C. 2005, ApJ, 629, 680

Hutchings, J. B., & Neff, S. G. 1987, AJ, 93, 14

Jiang, P., Zhou, H., Ji, T., et al. 2013, AJ, 145, 157

Just, D. W., Brandt, W. N., Shemmer, O., et al. 2007, ApJ, 665, 1004

Karakas, A. I. 2010, MNRAS, 403, 1413

Kishimoto, M., Hönig, S. F., Antonucci, R., et al. 2009, A&A, 507, L57

—. 2011, A&A, 536, A78

Kishimoto, M., Hönig, S. F., Beckert, T., & Weigelt, G. 2007, A&A, 476, 713

Kollatschny, W., Dietrich, M., & Hagen, H. 1992, A&A, 264, L5

Korista, K., Baldwin, J., Ferland, G., & Verner, D. 1997, ApJS, 108, 401

Korista, K. T., Bautista, M. A., Arav, N., et al. 2008, ApJ, 688, 108

Kraft, R. P. 1994, PASP, 106, 553

Landt, H., Bentz, M. C., Ward, M. J., et al. 2008, ApJS, 174, 282

Landt, H., Ward, M. J., Peterson, B. M., et al. 2013, MNRAS, 432, 113

Leighly, K. M. 2004, ApJ, 611, 125

Leighly, K. M., Dietrich, M., & Barber, S. 2011, ApJ, 728, 94

Leighly, K. M., Halpern, J. P., Jenkins, E. B., & Casebeer, D. 2007, ApJS, 173, 1

Leighly, K. M., Hamann, F., Casebeer, D. A., & Grupe, D. 2009, ApJ, 701, 176

Leighly, K. M., Kay, L. E., Wills, B. J., Wills, D., & Grupe, D. 1997, ApJ, 489, L137

Lípari, S., Terlevich, R., Zheng, W., et al. 2005, MNRAS, 360, 416

Lucy, A. B., Leighly, K. M., Terndrup, D. M., Dietrich, M., & Gallagher, S. C. 2014, ApJ, 783, 58

Luo, B., Brandt, W. N., Alexander, D. M., et al. 2013, ApJ, 772, 153

Maraston, C. 2005, MNRAS, 362, 799

Marconi, A., Schreier, E. J., Koekemoer, A., et al. 2000, ApJ, 528, 276

Martins, L. P., Rodríguez-Ardila, A., Diniz, S., Gruenwald, R., & de Souza, R. 2013, MNRAS, 431, 1823

Ogle, P. M., Cohen, M. H., Miller, J. S., et al. 1999, ApJS, 125, 1

Osterbrock, D. E., & Ferland, G. J. 2006, Astrophysics of gaseous nebulae and active galactic nuclei

Piconcelli, E., Miniutti, G., Ranalli, P., et al. 2013, MNRAS, 428, 1185

Pogge, R. W., Depoy, D. L., Atwood, B., et al. 1998, in Society of Photo-Optical Instrumentation Engineers (SPIE) Conference Series, Vol. 3354, Infrared Astronomical Instrumentation, ed. A. M. Fowler, 414–418

Popović, L. Č. 2003, ApJ, 599, 140

Rayner, J. T., Toomey, D. W., Onaka, P. M., et al. 2003, PASP, 115, 362

Richards, G. T., Lacy, M., Storrie-Lombardi, L. J., et al. 2006, ApJS, 166, 470

Rodríguez Zaurín, J., Tadhunter, C. N., & González Delgado, R. M. 2009, MNRAS, 400, 1139

Rudy, R. J., Stocke, J. T., & Foltz, C. B. 1985, ApJ, 288, 531

Rupke, D. S., Veilleux, S., & Sanders, D. B. 2002, ApJ, 570, 588

—. 2005, ApJ, 632, 751

Rupke, D. S. N., & Veilleux, S. 2011, ApJ, 729, L27

Sabra, B. M., & Hamann, F. 2001, ApJ, 563, 555

—. 2005, ArXiv Astrophysics e-prints

Salpeter, E. E. 1955, ApJ, 121, 161

Sanders, D. B., Soifer, B. T., Elias, J. H., Neugebauer, G., & Matthews, K. 1988, ApJ, 328, L35

Savage, B. D., & Sembach, K. R. 1991, ApJ, 379, 245

Schmidt, G. D., & Miller, J. S. 1985, ApJ, 290, 517

Smith, P. S., Schmidt, G. D., Allen, R. G., & Angel, J. R. P. 1995, ApJ, 444, 146

Tacconi, L. J., Genzel, R., Lutz, D., et al. 2002, ApJ, 580, 73

Teng, S. H., Brandt, W. N., Harrison, F. A., et al. 2014, ApJ, 785, 19

Trump, J. R., Hall, P. B., Reichard, T. A., et al. 2006, ApJS, 165, 1

Urrutia, T., Becker, R. H., White, R. L., et al. 2009, ApJ, 698, 1095

Vacca, W. D., Cushing, M. C., & Rayner, J. T. 2003, PASP, 115, 389

Veilleux, S., Trippe, M., Hamann, F., et al. 2013, ApJ, 764, 15

Véron-Cetty, M.-P., Joly, M., & Véron, P. 2004, A&A, 417, 515

Voit, G. M., Weymann, R. J., & Korista, K. T. 1993, ApJ, 413, 95

Wang, L. 2005, ApJ, 635, L33

Wills, B. J., Wills, D., Evans, II, N. J., et al. 1992, ApJ, 400, 96

Wilson, J. C., Henderson, C. P., Herter, T. L., et al. 2004, in Society of Photo-Optical Instrumentation Engineers (SPIE) Conference Series, Vol. 5492, Ground-based Instrumentation for Astronomy, ed. A. F. M. Moorwood & M. Iye, 1295–1305

Witt, A. N., Thronson, Jr., H. A., & Capuano, Jr., J. M. 1992, ApJ, 393, 611

Zheng, W., Kriss, G. A., Telfer, R. C., Grimes, J. P., & Davidsen, A. F. 1997, ApJ, 475, 469

This manuscript was prepared with the AAS LaTeX macros v5.2.